UNIVERSITY OF AMSTERDAM

UvA-DARE (Digital Academic Repository)

Laser diffraction microscopy

Schall, P.

DOI
10.1088/0034-4885/72/7/076601
Publication date
2009
Document Version
Author accepted manuscript
Published in
Reports Progress Physics

Link to publication

Citation for published version (APA):
Schall, P. (2009). Laser diffraction microscopy. *Reports Progress Physics*, *72*(7), 076601. https://doi.org/10.1088/0034-4885/72/7/076601

General rights
It is not permitted to download or to forward/distribute the text or part of it without the consent of the author(s) and/or copyright holder(s), other than for strictly personal, individual use, unless the work is under an open content license (like Creative Commons).

Disclaimer/Complaints regulations
If you believe that digital publication of certain material infringes any of your rights or (privacy) interests, please let the Library know, stating your reasons. In case of a legitimate complaint, the Library will make the material inaccessible and/or remove it from the website. Please Ask the Library: https://uba.uva.nl/en/contact, or a letter to: Library of the University of Amsterdam, Secretariat, P.O. Box 19185, 1000 GD Amsterdam, The Netherlands. You will be contacted as soon as possible.

UvA-DARE is a service provided by the library of the University of Amsterdam (https://dare.uva.nl)

Download date:13 Sept 2026

Final peer-reviewed manuscript of

Rep. Prog. Phys. 72 (2009) 076601 (34pp)
Laser diffraction microscopy
P Schall
doi:10.1088/0034-4885/72/7/076601
http://dx.doi.org/10.1088/0034-4885/72/7/076601
© 2009 IOP Publishing Ltd

Final peer-reviewed manuscript has been downloaded
from UvA-DARE: http://dare.uva.nl/record/337495

Laser diffraction microscopy

P Schall

Van der Waals-Zeeman Institute, University of Amsterdam, Valckenierstraat 65, 1018XE Amsterdam, The Netherlands.

E-mail: P.Schall@uva.nl

Abstract

Crystals composed of micrometer size colloidal particles diffract light and are both of fundamental interest as well as have important applications as filters, sensors and photonic devices. Laser light is used to diffract from these crystals in close analogy to x-ray or electron diffraction used for atomic crystals. Laser diffraction microscopy explores optical diffraction contrast to image crystals and crystal defects in analogy to the transmission electron microscopy technique used to image their atomic counterparts. This review discusses the application of optical diffraction contrast imaging to elucidate colloidal crystal nucleation and growth, and defect propagation. Diffraction contrast is described in terms of optical scattering theory and kinematical diffraction contrast theory developed for electron microscopy. Complementary information at the particle scale is obtained with high-resolution confocal microscopy. Confocal image stacks provide insight into the three-dimensional topology of defects and the interplay between applied strain and thermal fluctuations that governs defect nucleation.

PACS: 61.72.-y, 61.72.Dd, 61.72.Ff, 61.72.Hh, 62.20.F-, 68.37.Lp, 68.55.Ln, 82.70.Dd, 46.70.-p

Keywords: Colloids, Light diffraction, Crystal defect, Dislocation, Confocal microscopy, Transmission Electron Microscopy

Contents

1. Introduction
2. Imaging colloidal crystals
    2.1 Colloidal crystals and diffraction of light
    2.2 Imaging crystal morphologies
    2.3 Imaging crystal defects
    2.4 Imaging of colloidal crystals at the particle scale
    2.5 Principal of image formation: two-dimensional example
3. Theory of image contrast
    3.1 Scattering of light by small particles
    3.2 Diffraction from colloidal crystals
        3.2.1 Kinematical diffraction theory
        3.2.2 Dynamical diffraction
        3.2.3 Diffraction patterns
    3.3 Kinematical theory of image contrast
        3.3.1 Diffraction contrast images of perfect crystals
        3.3.2 Diffraction contrast produced by dislocations
4. Laser Diffraction Microscopy of dislocations in colloidal single crystals
    4.1 Colloidal single crystals
    4.2 Imaging of dislocations
    4.3 Imaging of dislocation propagation
        4.3.1 Dislocation motion
        4.3.2 Dislocation nucleation
5. Confocal microscopy of defects
    5.1 Dislocation topology
    5.2 Strain distribution
    5.3 Thermally activated defect nucleation
6 Simulation of diffraction image contrast of dislocations
    6.1 Image simulation techniques
    6.2 LDM image simulations
7. Conclusion

Acknowledgements
References

1. Introduction

The crystalline state is of fundamental importance to soft matter physics. Regular arrangements, “crystals”, form spontaneously in suspensions of small nanometer to micrometer size colloidal particles, driven by their Brownian motion, and by the interaction between the particles. These crystals are extremely soft and can be disrupted easily; yet, they exhibit similarities to their atomic counterpart that are of fundamental interest.

Because of the size of the constituent particles, colloidal crystals diffract light in the visible range, making them shine with bright iridescent colors (figure 1.1). Naturally produced opals give beautiful evidence of this diffraction of light at ordered arrangements of uniform silica particles, several hundred nanometers in diameter (Sanders 1964, Iler 1965). Viruses and proteins, genuinely uniform in their size, are other examples of naturally crystallizing suspensions (Bawden *et al.* 1936, Bernal and Fankuchen 1937). Since more than four decades, perfectly uniform particles with tailored sizes and shapes are synthesized in the laboratories, and the colorful iridescence of these suspensions gives still evidence of the ordered periodic arrangement of the particles. One uses laser light scattered from these crystals to determine the crystal structure in close analogy to x-ray and electron scattering of conventional crystalline materials. What fascinates us is that at the length scale of the colloidal particles, diffraction of light is directly discernible, making the relation between crystal structures and the observed scattered intensities most evident to our eyes.

Even more so: The use of visible light allows direct imaging of colloidal crystals with optical techniques. Individual crystallites are readily observable with the naked eye by their diffraction of light, and crystal images down to the scale of the individual particles are obtained with optical microscopy. These images provide direct insight into crystal nucleation and growth, and defect formation. A particular way of imaging is achieved when the crystal is oriented in a way that strong diffraction occurs at a single set of lattice planes. In this orientation, perfect crystal regions can be distinguished from distorted regions by their diffraction of light: Perfect crystal regions diffract strongly and appear bright, whereas distorted regions scatter less light and appear dark. This effect allows for imaging the morphology of crystals and their internal defect structure.

Conventional transmission electron microscopy (TEM) provides just such an imaging of defects for ordinary crystals. This technique, in which a coherent electron beam is scattered at a crystal to produce a real-space image that yields information about crystal lattice distortions, has greatly contributed to our knowledge of crystal defects. Of particular importance are dislocations, one-dimensional defects in the crystal lattice (Taylor 1934), that are central to our understanding of yield, fracture and fatigue of crystalline solids. Numerous studies have elucidated the relation between dislocation structures and mechanical properties of crystalline materials after mechanical loading, heat treatment and irradiation. TEM has played an important role in imaging defect structures. Together with theories of diffraction contrast, TEM is able to distinguish defect types and topologies. Improved understanding of dislocation formation, propagation and interactions has largely contributed to the development of new crystalline materials with tailored mechanical properties, thereby driving progress in materials science and development.

Laser diffraction microscopy (LDM) provides an analogous imaging technique for soft matter research (Schall *et al.* 2004). Coherent laser light is scattered at ordered assemblies of micrometer-size constituent units of soft matter to produce real-space images that highlight crystal lattice distortions. These images elucidate the formation, propagation and interaction of defects in soft crystals. The application of visible light allows regular light optics to be

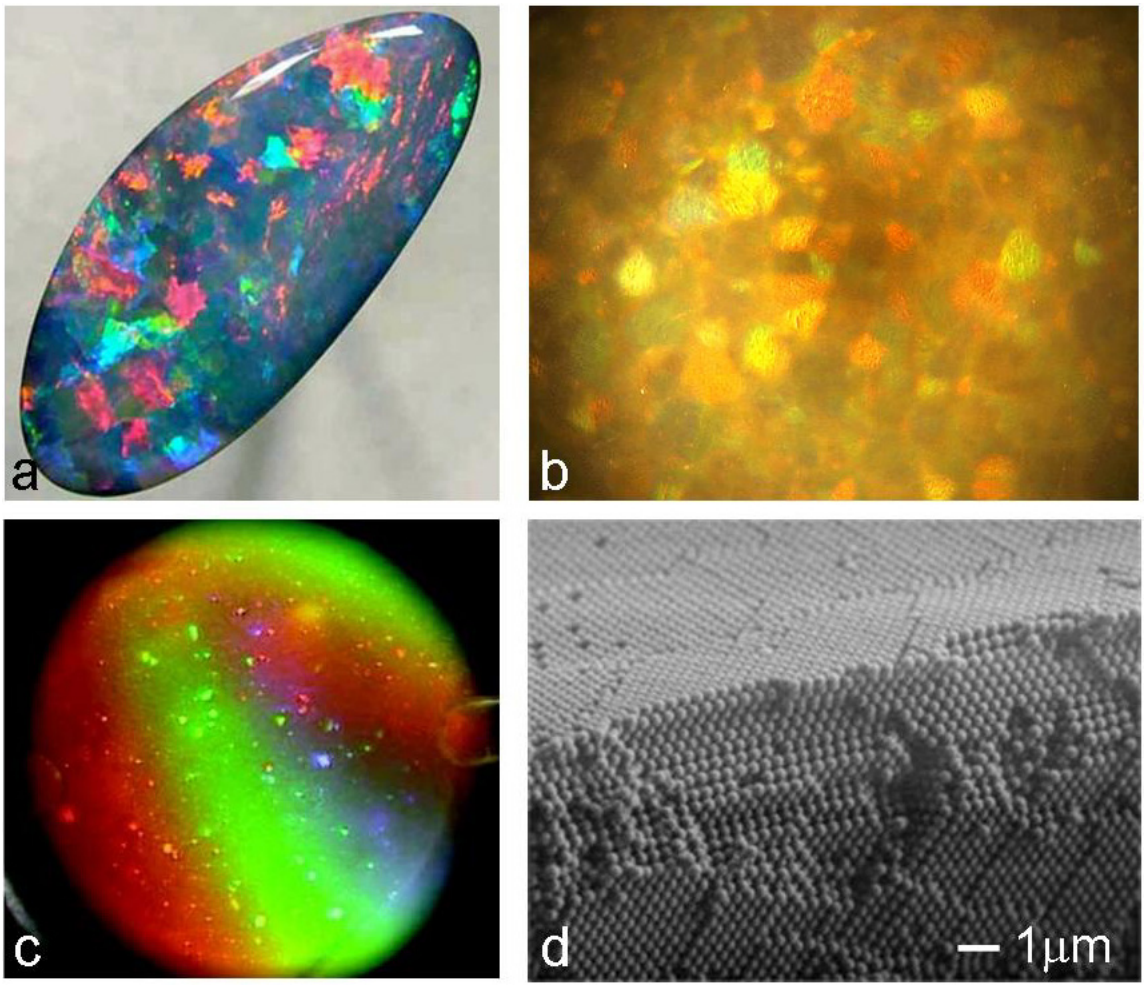

Figure 1.1 Colourful iridescence observed at an opal (a) and at crystallizing colloidal suspensions (b), (c) This iridescence is caused by the diffraction of light at a highly ordered arrangment of particles on micrometer length scales (d, scanning electron microscope image). Courtesy of Naturalgems.ch (a), D.A. Weitz (b), P. Chaikin (c), and P.J. Vancso (d).

used, which provide excellent imaging quality at low cost. Optical diffraction imaging uses low magnification lenses to obtain images of crystal defects on medium-range length scales. Complementary information at the single particle level is obtained with high-resolution optical microscopy. Confocal microscopy provides images of the individual particles in three dimensions that allow reconstruction of three-dimensional crystal sections. Together, LDM and confocal microscopy allow investigation of defect structures and defect propagation on a range of length scales. The combination of both techniques to elucidate crystal growth and defect propagation in colloidal crystals is a central part of this review.

The paper is organized as follows: Chapter 2 starts with a brief historical review of the application of light scattering to the investigation of colloidal crystals, their structure and elastic properties. Diffraction images were first obtained with ambient light. These images gave early evidence of dislocations in colloidal crystals, and provided insight into crystal growth. High-resolution optical microscopy provides images of crystal defects at the particle scale. A connection between diffraction contrast and conventional microscopic imaging is established in terms of the theory of wave-optical imaging, and a brief introduction into this formalism will conclude chapter 2.

Chapter 3 presents a quantitative description of optical diffraction contrast. Several theories of diffraction image contrast have been developed for transmission electron microscopy, and the simplest of these, kinematical diffraction theory, is presented here. The

application to the diffraction of light needs optical scattering theory, which will be introduced in simple terms in section 3.1. Kinematical diffraction theory uses concepts of lattice planes and the reciprocal lattice, which will be described and applied to colloidal crystals in 3.2. In addition to the predicted diffraction peaks, real diffraction patterns exhibit a diffuse background associated with inelastic scattering, and 'Kossel lines' resulting from the Bragg scattering of the diffusely scattered light. Applications of these Kossel lines to the study of colloidal crystals will be given. Chapter 3 will conclude with a description of the kinematical theory of diffraction image contrast developed for electron microscopy.

Chapter 4 describes the LDM imaging of dislocations in colloidal crystals. LDM images give access to important parameters of dislocation arrays, such as the density of dislocations, their Burgers vector, and line directions. Time series of these images reveal the propagation of dislocations. We will use continuum models to describe the lattice resistance to dislocation motion.

Chapter 5 discusses high-resolution optical microscopic imaging of colloidal crystal defects. Confocal microscopy allows reconstruction of the three-dimensional defect topology and the three-dimensional strain distribution. These microscopic observations provide a unique opportunity to test the applicability of continuum models at small length scales. Time series of confocal image stacks allow resolution of individual, thermally driven defect nucleation events, which offer insight into the interplay between applied strain and thermal fluctuations.

Finally, chapter 6 provides a direct link between the medium-range length scale of LDM and the particle scale exploited with confocal microscopy: We apply kinematical diffraction theory to simulate LDM image contrast from three-dimensional reconstructions of crystal defects. Kinematical diffraction theory is able to account for basic features of defect contrast such as its width and visibility.

2. Imaging colloidal crystals

Images of colloidal crystals are easily obtained: Individual crystallites are readily distinguishable with the naked eye from their diffraction of light that gives rise to strong iridescent colors. Opals give beautiful evidence of this scattering of light at periodic arrangements of naturally grown silica particles, which exhibit surprising uniformity in their size (Sanders 1964). Nowadays, particles with excellent precision in their size and shape are obtained routinely in the laboratories, and these particles form crystals with a high degree of perfection. When these crystals are illuminated with a collimated beam of coherent, monochromatic light, well-defined diffracted beams are observed that reveal the perfect structure of these crystals. In analogy to x-ray and electron diffraction of conventional crystalline materials, the angles between the incident and diffracted beams indicate the orientation and separation of crystal lattice planes. Kinematical and dynamical theories of x-ray diffraction have been applied to describe the scattering of light at colloidal crystals and to determine the average crystal structure from the observed diffracted beam intensities. The use of visible light offers the advantage that diffraction experiments can be performed most conveniently under ambient conditions and lasers provide light sources with excellent collimation and coherence.

Furthermore, conventional light optics provide direct images of these crystals down to the scale of the individual particles. Low magnification lenses provide an overview over crystal morphologies and defect arrangements. When the crystals are close to diffracting orientations, these images exhibit a pronounced contrast that demarcates perfect and distorted crystal regions. High magnification lenses, on the other hand, offer insight into the crystal structure and dynamics at the particle scale. For both imaging techniques, the same principle of image formation applies. The image is formed from a range of diffracted beams of the object that are collected by the lens. Laser diffraction and conventional microscopic imaging differ in the size and orientation of the range of collected diffracted beams, selected by the size and position of the aperture of the imaging lens.

While the principles of image formation and the fundamental limitations of optical imaging are treated in various textbooks on optics, we will focus on the particular aspect of imaging crystals – regular arrangements of scatterers that give rise to discrete diffracted beams associated with the crystal lattice planes.

2.1 Colloidal crystals and diffraction of light

Diffraction of visible light at colloidal crystals has been used since the early days of soft matter science to elucidate colloidal crystal structures (Williams and Crandal 1974, Clark *et al.* 1979, Pieranski *et al.* 1981). Colloidal crystal planes with separation d cause scattering of the incident light at angles θ defined by the Bragg condition

$$2\,d\sin\theta = m\,\lambda', \qquad (2.1a)$$

where m is an integer number and λ' is the wavelength of the light *within* the suspension, which is given by

$$\lambda' = \lambda_0 / n_s, \qquad (2.1b)$$

where λ_0 is the wavelength in air, and n_s is the refractive index of the suspension (Luck 1963a,b, Hiltner and Krieger 1969). The modified Bragg condition (2.1) for colloidal crystals was verified experimentally by using a tungsten lamp attached to an x-ray goniometer setup to measure scattering angles of crystals composed of polystyrene particles (Hiltner and Krieger 1969). These particles provided an early model system to study colloidal crystallization. Suspended in an aqueous solvent, these particles are typically charged, and they form crystals

at low particle concentrations due to the repulsive interaction between the particles. Similarly to x-ray and electron diffraction for ordinary crystals, crystal structures have been identified from the arrangement of diffraction spots. Charged polystyrene particles were observed to form body-centered cubic (bcc) crystals at low, and face-centered cubic (fcc) crystals at high particle concentrations (Williams and Crandal 1974, Sirota *et al.* 1989, Monovoukas and Gast 1989). The spacing between crystal planes has been determined from the measured diffraction angles using Bragg's law. Light scattering measurements were used to determine the melting temperature and corresponding enthalpy of melting of these crystals. Values of the order of a few kcal per Mol were obtained (Williams *et al.* 1976), similar to those of atomic crystals. Light scattering has also been applied to measure the crystals´ elastic moduli (Crandall and Williams 1977, Dubois-Violette *et al.* 1980). From the shift of Bragg positions of crystals compressed under their own weight, Crandall and Williams determined elastic moduli of the order of 0.1 to 0.3 Pa, roughly 11 orders of magnitude smaller than those of atomic crystals. Values of the same order have been obtained by more precise mechanical oscillatory measurements (Mitaku *et al.* 1978, Lindsay and Chaikin 1982) and simulations (Frenkel and Ladd 1987). Hence, these crystals are extremely soft, and can be easily destroyed by slight agitation of the samples.

Hard-sphere particles, realized experimentally through short-range repulsive particle interactions, form close-packed crystals only (Pusey and van Megen 1986, Hoover and Ree 1967). The important parameter that determines the fluid-crystal transition is the particle volume fraction, defined by the volume of the particles divided by the total volume of particles and solvent. This parameter plays the role of inverse temperature: hard-sphere fluids at volume fractions above ϕ_f=0.49 crystallize, whereas hard-sphere crystals at volume fractions below ϕ_m=0.54 melt. ϕ_f and ϕ_m define the freezing and melting volume fractions, respectively.

Randomly nucleated hard-sphere crystals consist of two-dimensional hexagonal close-packed (hcp) layers that are stacked randomly in the A, B and C positions of the hexagonal plane. One can consider these as face-centered cubic (fcc) or hcp crystals that are heavily faulted on, respectively, a (111) or the (0001) basal plane. Since next nearest-neighbor interactions are negligible in hard-sphere systems, the energy difference between fcc and hcp is vanishingly small (Pronk and Frenkel 1999) and stacking faults form easily. Diffraction patterns of these crystals consist of a superposition of Bragg reflections from the close-packed planes and a structured diffuse background associated with the random stacking of these planes (Edwards and Lipson 1942, Wilson 1942). Light scattering has been used to determine the stacking probability α with which adjacent planes exhibit fcc-type stacking (Pusey *et al.* 1989). Values of $\alpha \approx 0.5$ have been found, which indicate complete random stacking.

2.2 Imaging crystal morphologies

Images of Bragg diffracted light, in which iridescent colors demarcate crystalline regions, can be readily observed with the naked eye - appealing and easily accessible with visible light for colloidal crystals, but prohibitively difficult with x-rays for atomic crystals. In their influential paper in 1986, Pusey and van Megen used images of samples prepared at increasing particle volume fractions to illustrate the phase diagram of hard-spheres: Iridescent colors that emerged from a uniformly scattering phase at increasing particle volume fraction showed the emergence of a crystalline phase from the isotropic fluid phase. By determining the relative amount of crystal and fluid phases, the authors verified the phase boundaries of the fluid-crystal coexistence region, $\phi_f = 0.49$ at freezing and $\phi_m = 0.54$ at melting, experimentally.

Images of light scattered from individual crystallites offer direct insight into the nucleation and growth of these crystals. In their pioneering studies, Aastuen *et al.* (1986) used

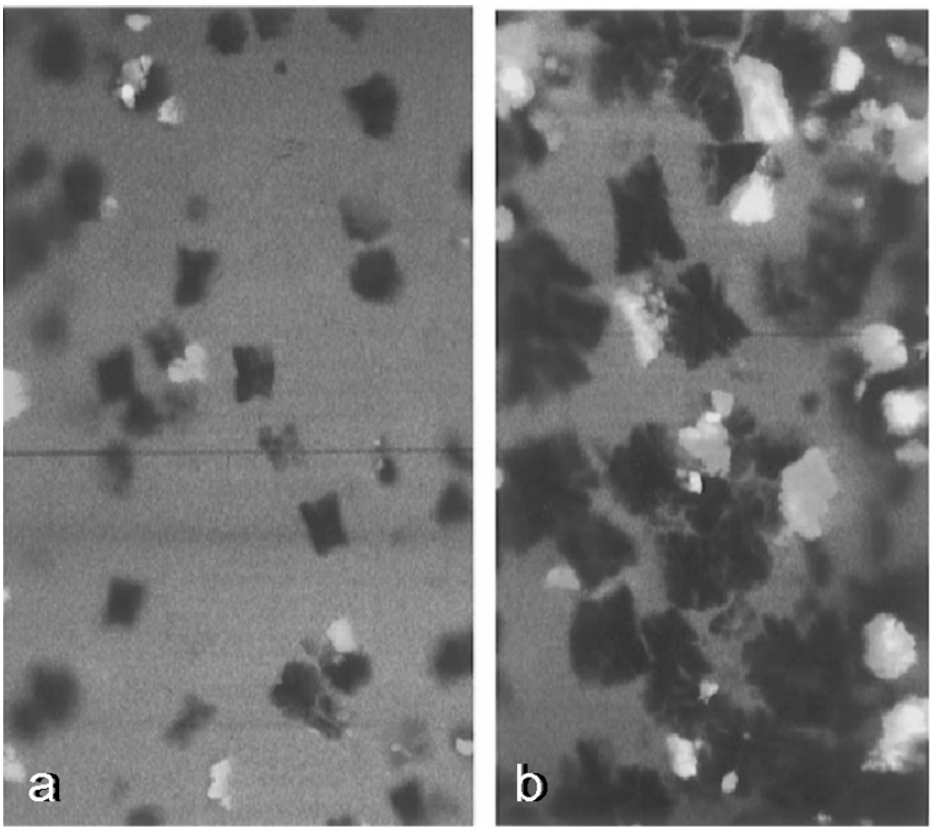

Figure 2.1 Photographs of dark and Bragg scattering (white) hard sphere colloidal crystals in a colloidal fluid (grey). Pictures are taken 135 min (a) and 242 min (b) after melting (He *et al.* 1997).

white light to visualize the morphology of growing crystals and determine their growth velocity. The system consisted of charged polystyrene spheres suspended in water. The crystals that grew from the colloidal fluid phase exhibited a round, non-facetted shape. The crystal size increased linearly with time, with growth velocities as large as 20 μms^{-1} at high particle concentrations. The authors concluded that the crystals grow as fast as they can, only limited by free-particle diffusion to the interface of the growing crystal. An overview over crystal morphologies in charged-sphere systems is given by Okuba (1994). Beautiful images obtained with white light illumination elucidate the relation between crystal morphology and particle charge.

The use of monochromatic light allows imaging with even better contrast. He *et al.* (1997) used monochromatic light to elucidate the rough morphology of growing hard-sphere crystals. A camera placed at the first-order Bragg angle collected the Bragg diffracted light to obtain images, in which crystals appear either bright or dark (figure 2.1). Crystals that are in Bragg orientation diffract light in the direction of the camera and appear bright, whereas crystals that are not in Bragg orientation scatter less light in the direction of the camera than the surrounding disordered fluid phase and appear dark. These images provide excellent contrast that is well suited for tracing crystal morphologies. The crystals showed rectangular shapes and protrusions around 100 μm wide. These morphologies indicate the emergence of a dendritic growth instability in hard-sphere suspensions. This growth instability is found to be even more pronounced when the influence of gravity is turned off: colorful photographs taken on board the space shuttle of a crystallizing colloidal suspension reveal crystals 2 mm in size with pronounced dendrites roughly 100 μm wide (Zhu *et al.* 1997). A linear stability analysis formulated for diffusion-limited growth can account for this dendritic instability, and suggests an intermediate regime for the growth (Russel *et al.* 1997). This analysis establishes a relation between hard-sphere and molecular crystal growth.

Figure 2.2 Colloidal polycrystal viewed between crossed polarizers
Grey tones indicate crystal orientation and lattice constant. Striations within crystallites indicate twinning of the fcc lattice (Monovoukas and Gast 1991).

Other methods that take advantage of the Bragg scattering of light to image crystal morphologies include the use of crossed polarizers to highlight ordered crystal regions. Because the diffraction of light by the crystal depends on the polarization direction of the light with respect to the orientation of the primary diffraction planes, the transmitted light is attenuated anisotropically, depending on the polarization direction (Monovoukas *et al.* 1990b). As the sample is viewed between crossed polarizers, crystallites become visible from the color and intensity of the transmitted light (figure 2.2). Both depend on the crystal orientation and lattice constant. This imaging technique has been used to elucidate crystal morphologies in charged colloidal systems (Monovoukas and Gast 1990a, 1991). It has revealed a dendritic growth instability in these long-range repulsive systems (Gast and Monovoukas 1991). At certain orientations of the crystals, striations occur as shown in figure 2.2. These striations indicate alternating crystal lattice orientations within the crystallites. Monovoukas and Gast (1991) attribute these to fcc twins within the fcc crystals.

2.3 Imaging crystal defects

He *et al.* (1997) point out that extensive contrast features are observed within crystals grown to larger size (figure 2.1b). They attribute these contrast features to the internal defect structure of the crystallites. Colloidal crystals exhibit defects just like ordinary crystals do, such as vacancies, dislocations and stacking faults (Pieranski 1981). These defects form easily, because colloidal crystals are genuinely soft. The elastic modulus and, consequently, the elastic limit of these crystals is roughly 11 orders of magnitude smaller than that of ordinary crystals. It can be estimated by a dimensional argument as U/a^3, where U is a typical interaction energy and a the separation between particles. For a hard-sphere colloidal

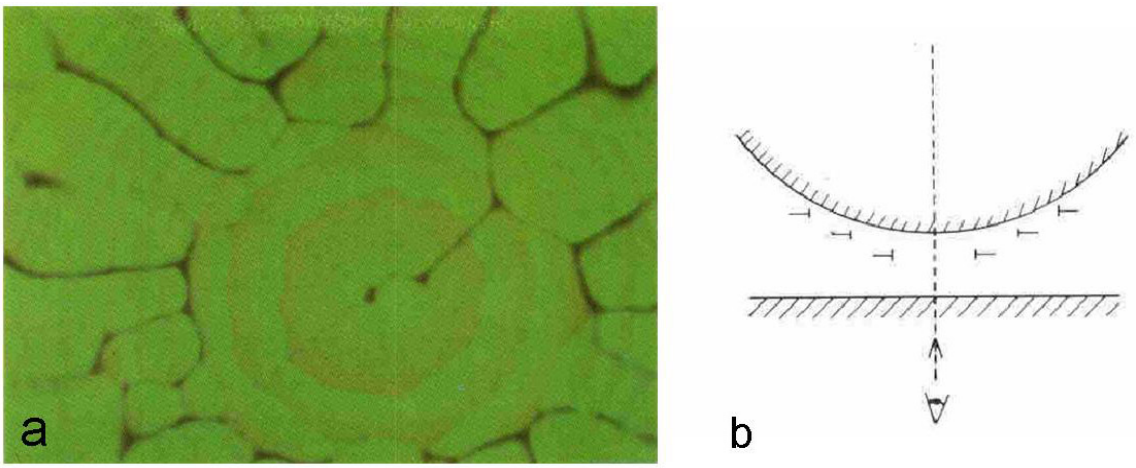

Figure 2.3 Edge dislocations below a spherical wedge
(a) Photograph of edge dislocations and grain boundaries. The concentric dislocation loops appear as discontinuities in the color of the reflected light; the internal edge of each dislocation loop is red (dilation of the colloidal crystal), while the external edge is green (compression of the crystal). The black radial streaks are grain boundaries between crystallites of different orientation. (b) Schematic of the dislocation arrangement. Edge dislocations (⊥) indicate the boundary of inserted planes necessary to fill the space between the spherical and plane boundaries (Pieranski 1983).

system with $a = 1\,\mu\text{m}$ this becomes $kT/1\,\mu\text{m}^3 \sim 1\,\text{Pa}$, while for an atomic system this gives $1\text{eV}/1\text{Å} \sim 100\,\text{GPa}$.

The extraordinarily low elastic modulus indicates that defects form easily in colloidal crystals. Of specific interest here are dislocations, line defects in the crystal lattice, as these defects play a central role in the mechanical behavior of crystalline materials. Their nucleation, propagation and interaction is central to the understanding of yield, fracture, and fatigue of conventional crystalline solids (Hirth and Lothe 1982). In colloidal crystals, the small stresses that are induced by shaking crystal samples gently in the hand may be large enough to introduce a large number of dislocations (Pieranski 1981). Similarly to ordinary crystals, dislocations in colloidal crystals have been identified from their diffraction contrast. Pieranski *et al.* (1979) have shown that under white light illumination, lattice distortions associated with dislocations give rise to color modulations in the images of Bragg diffracted light (figure 2.3a). Edge dislocations were induced by confining the crystals between a flat bottom and a spherical top plate to produce a wedge geometry. The dislocations form closed loops centered around the center of the spherical wedge as shown by the concentric red circles in figure 2.3a. Each edge dislocation marks the boundary of an inserted crystal layer. This observation is compatible with a simple model of edge dislocations that are necessary to accommodate the change of sample thickness under the wedge (figure 2.3b).

Another observation of dislocations is achieved at grain boundaries (figure 2.4). Small misorientations between neighboring crystal grains are accommodated by arrays of edge dislocations, in close analogy to small angle grain boundaries of ordinary crystals (Pieranski, 1981). In figure 2.4, these dislocations are visible as dark spots. Larger misorientations between grains are accommodated by continuous lattice distortions between the grains as shown by the dark boundaries in figure 2.4.

More quantitative information about the crystal lattice is obtained by using coherent laser light to image defects. A laser diffraction microscopy setup (Schall *et al.* 2004) is used in close analogy to the transmission electron microscopy technique to image dislocations in colloidal crystals (figure 2.5a). The light of a laser scatters coherently from the colloidal

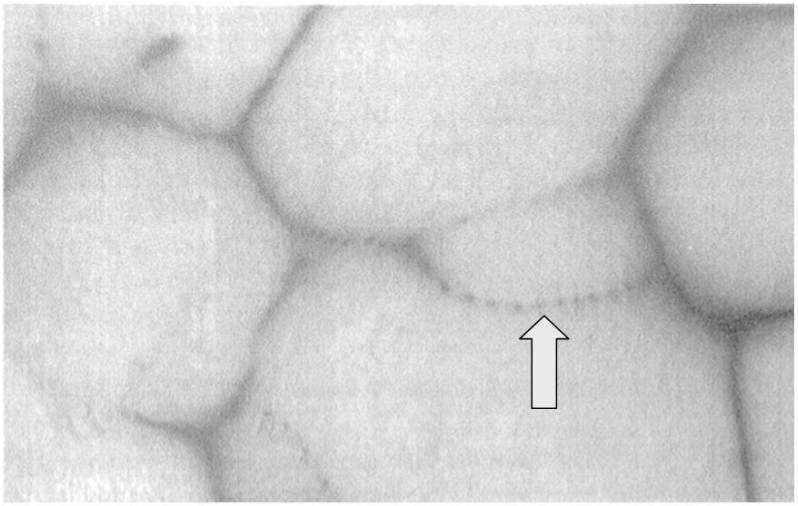

Figure 2.4 Photograph of grain boundaries in colloidal crystals
Arrays of black dots (arrow) indicate dislocations at small angle grain boundaries. Thick lines indicate boundaries between grains with strongly different orientations (Pieranski 1981).

crystal. Two lenses are used to project the light of the transmitted or one of the diffracted beams onto a screen. When the sample is tilted slightly so that the Bragg-condition for one set of crystal lattice planes is fullfilled, the intensity in the corresponding diffracted beam is maximized and dark lines appear in the image on the screen (figure 2.5b). These indicate crystal lattice distortions due to dislocations. The diffractive origin of this contrast is illustrated experimentally by contrast inversion: As the sample is tilted slightly further to decrease the intensity of the diffracted beam, the contrast on the screen inverts (figure 2.5c). Laser diffraction images of dislocations can be used to obtain information about the defect topology, and visualize defect propagation. Analogue images obtained with transmission electron microscopy have provided important insight into defect mechanisms in ordinary crystals, which are central to their mechanical properties. We will focus on the application of laser diffraction microscopy to study defect propagation in colloidal crystals in chapter 4.

2.4 Imaging colloidal crystals at the particle scale

The use of visible light to image colloidal crystals has another advantage: high numerical aperture lenses can be used, which allow resolution of individual colloidal particles with sizes larger than roughly 200 nm. This technique provides insight into colloidal crystals at the particle scale. Images of the crystal lattice are easily obtained for two-dimensional colloidal crystals that consist of only one crystalline layer. Direct imaging of the individual particles in the crystal layer provided insight into melting (Zahn and Maret, 2000), lattice vibrations (Zahn *et al.* 2003, Keim *et al.* 2004) and vacancy diffusion (Pertsinidis and Ling 2001a,b, 2005). Conventional microscopy has also been applied to obtain images of the particles in three-dimensional colloidal crystals (Kose *et al.* 1973, Murray and Grier 1996), but these observations are limited to the first few layers of the crystal. The problem is twofold: multiple scattering on the one hand, and the wide depth of focus on the other hand limit image contrast and make the imaging of particles deep in the bulk of dense suspensions prohibitively difficult. A recent review by Elliot and Poon (2001) discusses the limitations and possibilities of conventional optical microscopy techniques to image three-dimensional colloidal crystals.

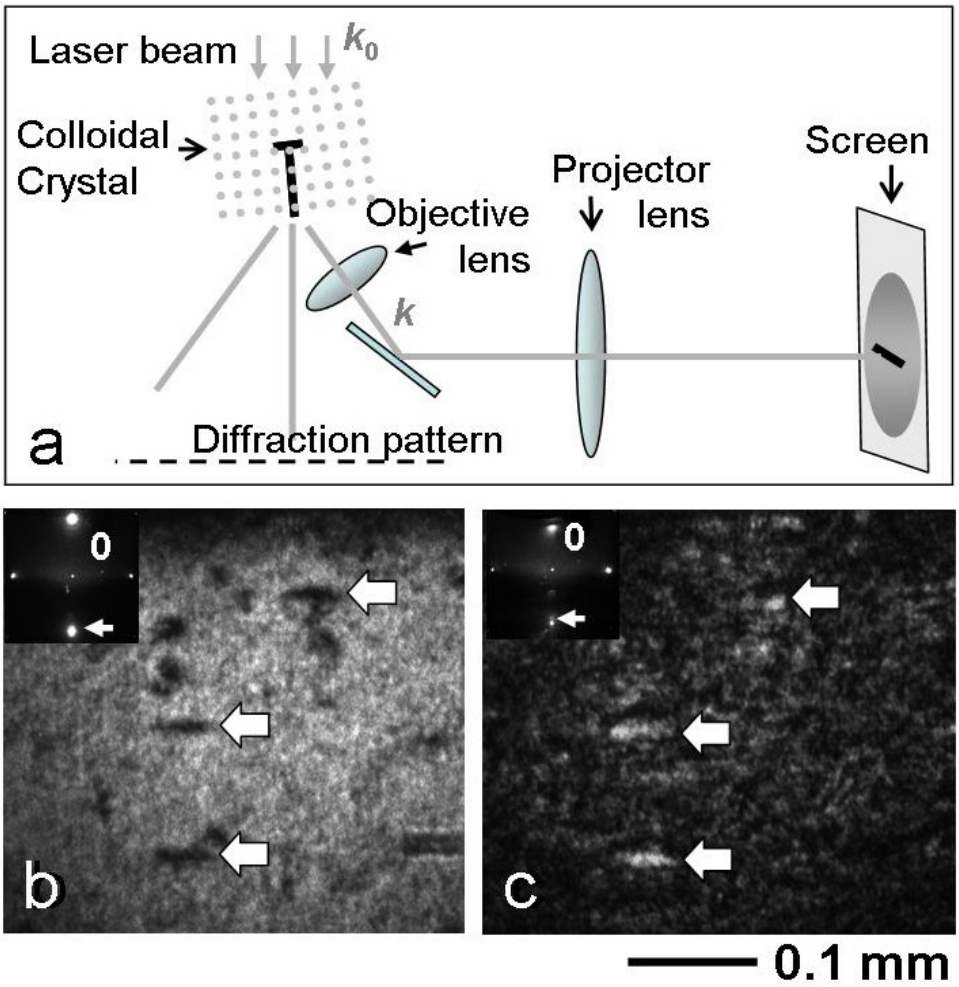

Figure 2.5 Laser diffraction microscope (LDM) and images of dislocations in colloidal crystals (a) Schematic of the LDM instrument: A laser beam is sent through the colloidal crystal. One of the diffracted beams is imaged on a screen by means of an objective and a projector lens. (b) and (c) LDM images of a colloidal crystal show dislocations (arrows). The inset shows the diffraction pattern from the crystalline film. 0 indicates the transmitted beam, and arrows indicate the diffracted beam used for imaging. (b) Sample in Bragg orientation resulting in a strong intensity in the diffracted beam. (c) Sample is tilted slightly so that the diffracted beam intensity decreases. This gives rise to an inversion of the image contrast. (Schall *et al.* 2004)

The limitations of conventional microscopy can be overcome by using confocal laser microscopy. This technique extends the range of optical microscopic imaging to somewhat smaller objects with three-dimensional imaging capability (Gu 1996, Sheppard and Shotton 1997). The improvement over conventional optical micoscopy is twofold (Minsky 1988): A pinhole aperture positioned at the image plane blocks light outside the focal plane and reduces the imaged volume to a thin slice, thereby increasing contrast and enabling sectioning of the sample to obtain three-dimensional images. Second, unlike conventional widefield optical microscopes, where the whole sample is illuminated at once, in confocal, a beam of laser light is scanned across the sample, and this point by point illumination minimizes scattered light. Due to the three-dimensional imaging capability and the improved resolution, confocal microscopy has become an invaluable tool in biology (Pawley 1995), materials and nanoscience (Lu 2005) and soft matter science (Prasad *et al.* 2007).

Among the first to use confocal microscopy to study the three-dimensional structure of colloidal crystals were Yoshida *et al.* (1991) and van Blaaderen *et al.* (1992). They pointed out that this technique allows imaging individual particles in the bulk of a colloidal sample far

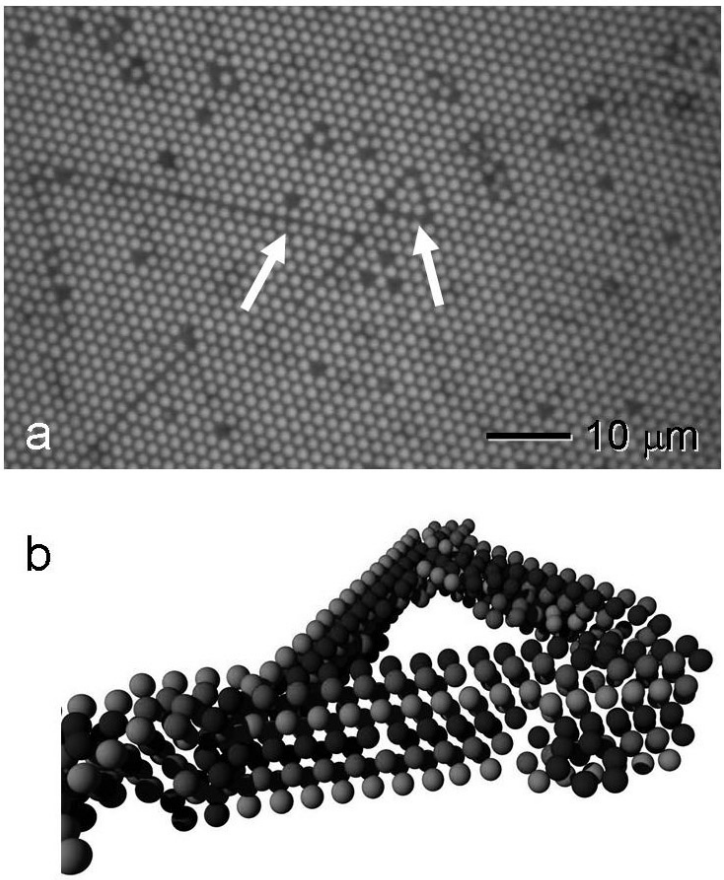

Figure 2.6 Stacking faults and vacancies in hard-sphere colloidal crystals
(a) Confocal microscope image of a hexagonal close-packed crystal plane that is intersected by stacking faults. (b) Three-dimensional reconstruction of a stacking fault configuration (Meijer *et al.* 2007).

away from the sample boundaries. Confocal microscopy has since then been used to elucidate the stacking order of hard sphere crystals (Verhaegh *et al.* 1995, Dolbnya *et al.* 2005, van Blaaderen *et al.* 1997), and the structure of various binary (Hunt *et al.* 2000, Schofield *et al.* 2005), and ionic crystals (Leunissen *et al.* 2005, Bartlett and Campbell, 2005). Ionic colloidal crystals are composed of two kinds of particles with opposite charge.

Recent fast confocal microscopes allow image acquisition at frame rates faster than video rate. Using image analysis software, particles can be located precisely in two and three dimensions (Crocker and Grier 1996, Dinsmore *et al.* 2001), and from a timeseries of microscope image stacks, particle motions can be tracked in three dimensions and with time (Weeks *et al.*, 2000). This offers a unqiue way to study the dynamics of condensed matter at the single particle level. This technique has been used to elucidate the structure (van Blaaderen and Wiltzius 1995) and dynamics of hard-sphere glasses (Weeks *et al.* 2000, Kegel and van Blaaderen 2000), crystal nucleation (Gasser *et al.* 2001), kinetics of phase transitions (Anderson and Lekkerkerker 2002), and interfaces and interface fluctuations (Aarts *et al.* 2004, Aarts *et al.* 2005, Dullens *et al.* 2006). In particular, it has led to new insight into non-equilibrium phenomena for which hard-sphere and attractive colloidal systems provide excellent model systems (Trappe *et al.* 2001, Pham *et al.* 2002, Campbell *et al.* 2005, Dinsmore *et al.* 2006, Lu *et al.* 2006, Simeonova *et al.* 2006). A recent paper by Prasad and Weeks (2007) reviews the application of confocal microscopy to study colloidal systems.

The three-dimensional imaging capability of confocal microscopy offers a unique opportunity for the investigation of crystal defects. Stacking faults and vacancies are readily

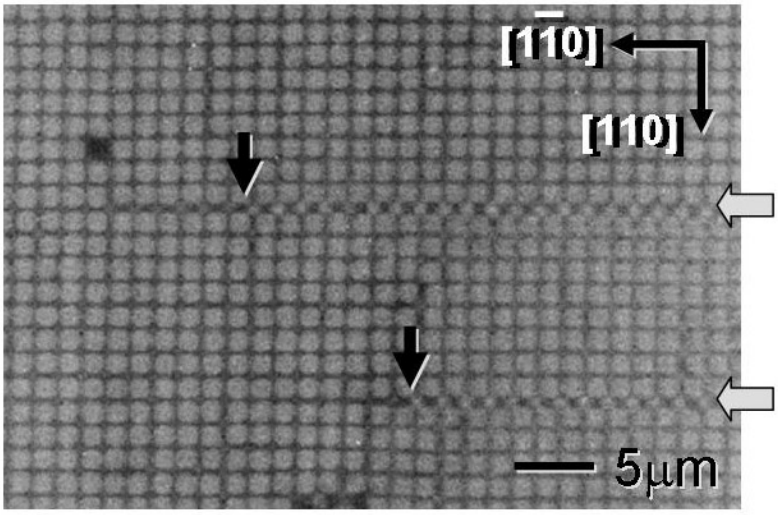

Figure 2.7 Screw dislocations that bound stacking faults in colloidal fcc crystals
Confocal microscope image of a (100) fcc plane intersects two screw dislocations that bound stacking faults (⇦) along hcp planes. Black arrows indicate the position of the dislocation core.

identified from confocal microscope images (figure 2.6a). Three-dimensional reconstructions of the stacking faults are obtained by identifying particles with distorted nearest neighbor configurations (figure 2.6b). This is achieved by using local bond order parameters that characterize the nearest neighbor vectors (Schall *et al.*, 2004, Meijer *et al.* 2007). These techniques are similar to those used in computer simulations of defects (Kelchner *et al.* 1998).

Stacking faults have been studied in hard-sphere crystals grown by sedimentation (Hoogenboom *et al.* 2002, Meijer *et al.* 2007 and de Villeneuve *et al.* 2007) and in crystals formed by shear (Solomon and Solomon 2006). As a pronounced feature, stacking faults are observed to form tetrahedral configurations as shown in figure 2.6. These remind of stacking fault tetrahedra observed in fcc metals with low stacking fault energy and after rapid quench or radiation damage (Hull and Bacon 2001, Kiritani 1997).

In pure fcc crystals, dislocations are frequently observed to bound stacking faults. This is shown for a (100) crystal plane in figure 2.7, where two stacking faults are bound by screw dislocations on the left side. Confocal microscopy reveals the three-dimensional displacement field associated with the dislocations: Particles close to the stacking faults are displaced within as well as out of the imaged plane, as shown by the slight blurriness of the particles. Hence, three-dimensional reconstructions of the crystal lattice give insight into the three-dimensional strain distribution associated with these defects. This will be demonstrated for long, straight dislocations as well as for dislocation loops in section 5.2.

2.5 Principle of image formation: two-dimensional example

While diffraction contrast techniques provide images on medium-range length scales, high-resolution techniques offer images with details down to the single particle level. In this section, we establish a relation between both types of imaging. This relation requires an introduction into the theory of wave-optical imaging (see e.g. Reimer 1993), which will be given in the following. We consider object points Q and an ideal lens that creates image points Q' of Q (figure 2.8). The object points Q emit rays in all directions. Parallel rays emitted from different object points intersect in the backfocal plane of the lens

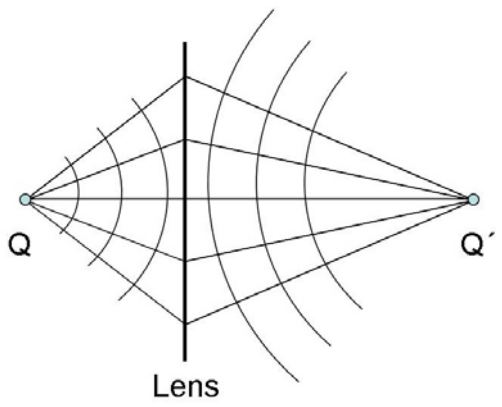

Figure 2.8 Image formation by a lens
The rays emitted by the object point Q are converged by the lens to intersect at the image point Q´. Circle sections indicate wavefronts of the corresponding spherical waves.

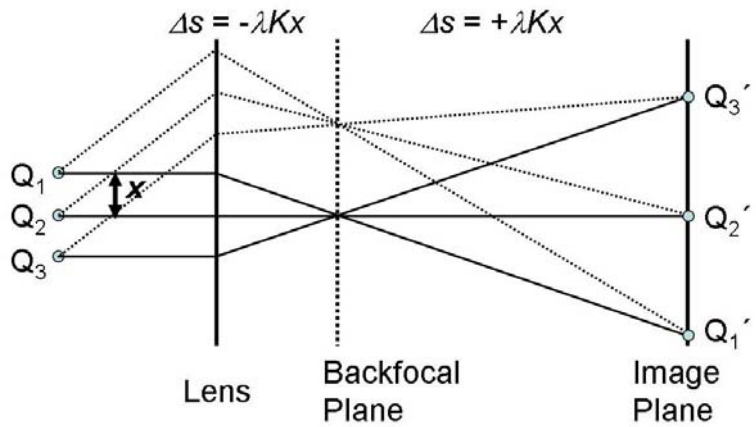

Figure 2.9 Beam paths and optical path differences produced by a lens
Shown are three object points Q_1,..., Q_3, their images Q_1´,..., Q_3´ and the paths of two representative beams emitted by each object point. Beams emitted in the same direction intersect in the backfocal plane of the lens. The separation x between object points results in the path differences $\Delta s = -\lambda Kx$ and $\Delta s = +\lambda Kx$ in front of and behind the backfocal plane.

(figure 2.9). Hence, this plane provides an image of the farfield of the object. It shows the distribution of the diffracted intensities far away from the object. To calculate the intensity distribution in this diffraction plane, we go over to the wave-optical formulation. Parallel beams are represented by plane waves with wavefronts orthogonal to the rays of geometric optics. We introduce the amplitude distribution $\psi_0(\boldsymbol{r})$ in the object plane, which represents the amplitudes of the waves emitted by the object points Q. The plane waves are written in the form

$$\psi = \psi_0(\boldsymbol{r})\, e^{2\pi i \boldsymbol{k}\boldsymbol{r}}, \qquad (2.3)$$

where the wave vector $\boldsymbol{k}$ is perpendicular to the wavefronts and has the magnitude $k = 1/\lambda$. All waves with parallel wave vectors interfere in the backfocal plane. Because the scattering at object points separated by $\boldsymbol{r}$ causes the optical path difference

$$\Delta s = -\lambda(\boldsymbol{k} - \boldsymbol{k_0})\, \boldsymbol{r}, \qquad (2.4)$$

where $\boldsymbol{k_0}$ and $\boldsymbol{k}$ are the wave vectors of the incident and scattered beams (figure 2.10), the corresponding waves exhibit the phase difference

$$\Delta\varphi = (2\pi/\lambda)\, \Delta s = -2\pi(\boldsymbol{k} - \boldsymbol{k_0})\, \boldsymbol{r}. \qquad (2.5)$$

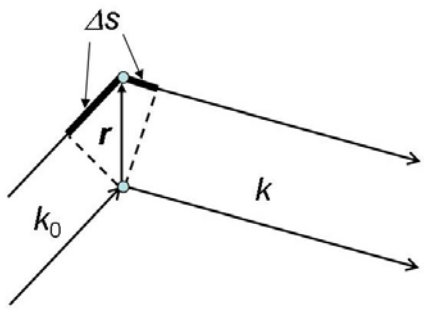

Figure 2.10 Path difference between diffracted beams
$\boldsymbol{k}_0$ and $\boldsymbol{k}$ are the wave vectors of the incident and diffracted beams. The separation $\boldsymbol{r}$ between object points gives rise to the optical path difference $\Delta s = (\boldsymbol{k}-\boldsymbol{k}_0)\boldsymbol{r}$.

We substitute the diffraction vector

$$\boldsymbol{K} = \boldsymbol{k} - \boldsymbol{k}_0, \tag{2.6}$$

which plays the role of a coordinate in the diffraction plane. $\boldsymbol{K}$ is related to the scattering angle θ by

$$|\boldsymbol{K}| = 2\,k\sin(\theta/2). \tag{2.7}$$

The amplitude $F(\boldsymbol{K})$ in the diffraction plane is obtained by the superposition of all waves with wave vector $\boldsymbol{k}$ taking into account the relative phases of the waves. We obtain

$$F(\boldsymbol{K}) = \iint_O \psi_0(\boldsymbol{r}) \exp(-2\pi i\,\boldsymbol{K}\boldsymbol{r})\, d^2r, \tag{2.8}$$

where the integration is performed over all points in the object plane O. $F(\boldsymbol{K})$ is the Fourier transform of the object amplitude distribution $\psi_0(\boldsymbol{r})$.

Let us now turn to the amplitude distribution ψ_i in the *image* plane. To form the image Q' of Q, an ideal lens introduces the phase shifts necessary to create a spherical wave beyond the lens that converges onto the image point Q' (figure 2.8). The phase shifts necessary for constructive interference at point Q' are

$$\Delta\varphi' = -\Delta\varphi = +2\pi\boldsymbol{K}\boldsymbol{r}. \tag{2.9}$$

The amplitude at Q' is obtained by the superposition of all waves that correspond to the vectors $\boldsymbol{K}$ in the diffraction plane, taking into account the phase differences introduced by the lens. The resulting amplitude at Q' is

$$\psi_i \propto \iint F(\boldsymbol{K}) \exp(+2\pi i\boldsymbol{K}\boldsymbol{r})\, d^2\boldsymbol{K}, \tag{2.10}$$

where the integration is performed over all elements of area $d^2\boldsymbol{K}$ in the diffraction plane. The right side of equation (2.10) represents the inverse Fourier transform of $F(\boldsymbol{K})$. Hence, the image amplitude distribution is given by the inverse Fourier transform of the amplitude distribution in the diffraction plane.

For a perfect lens, there will be no further phase shift, and the integration will be over the whole range of spatial frequencies that appear in the object. Real lenses, however, exhibit lens aberrations that introduce additional phase shifts, and a finite aperture that limits the range of spatial frequencies. We will neglect lens aberrations here, and consider only the effect of finite objective apertures. A lens with aperture α_0 captures only beams with scattering angles in the range

$$\theta < \theta_{max} = \alpha_0, \tag{2.11}$$

thereby limiting the range of spatial frequencies in the image to $K < K_{max}$. This limitation results in a loss of details in the image. To evaluate the effect of this limitation, we introduce

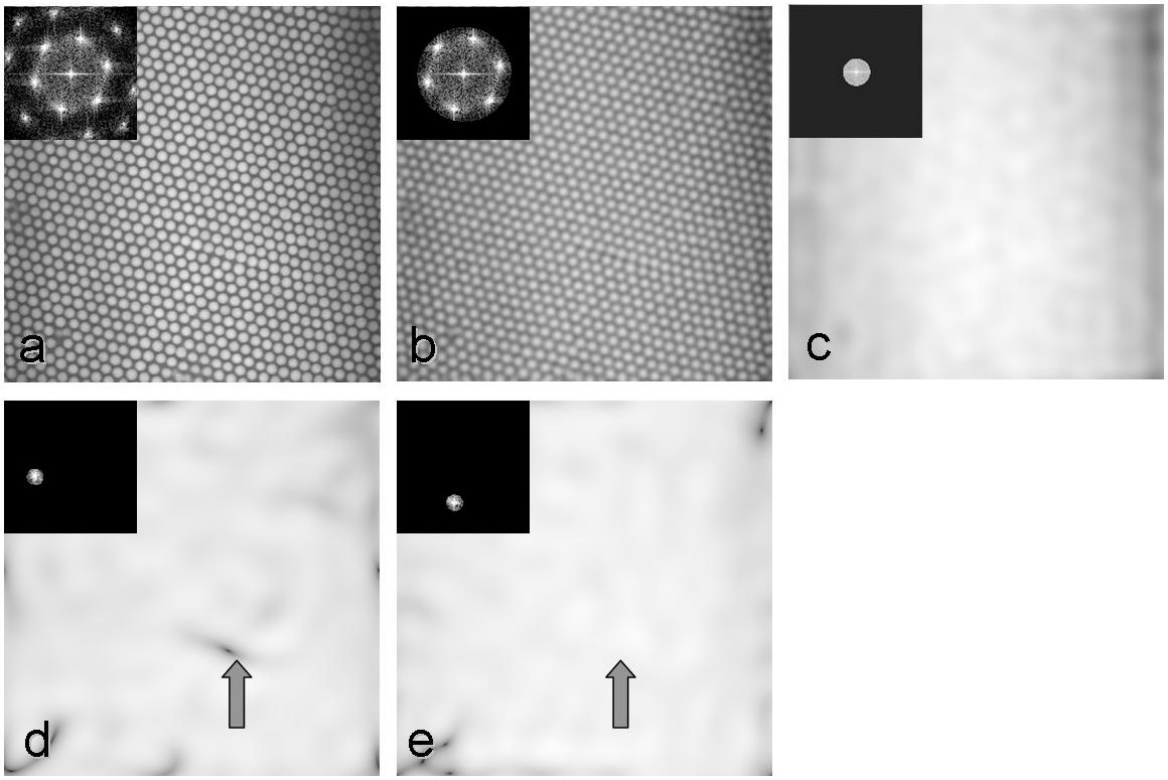

Figure 2.11 Illustration of image formation with different apertures and diaphragm positions
(a) Reference image showing a two-dimensional section through a colloidal crystal. The particles appear bright on a dark background. Inset: Intensity distribution in Fourier space shows the diffraction pattern of (a) as observed in the backfocal plane of a lens that images (a). (b)-(e) Images obtained by inverse Fourier transform of a limited range of Fourier space of (a). The intensity distribution in Fourier space used to calculate the image is shown in the inset of each image. (b) Image calculated from a section of Fourier space that includes the central six diffraction spots. (c) Image calculated from a smaller section of Fourier space that does not include the central six spots. The particles are no longer resolved. (d) Image calculated from a small section of Fourier space around a diffracted spot: Lattice distortions give rise to a dark contrast (arrow). (e) Image calculated from a small section of Fourier space around a diffracted spot with diffraction vector perpendicular to that used in (d): No contrast is observed.

the masking function $M(\boldsymbol{K})$, which is 1 for $K < K_{\max}$ and 0 for $K > K_{\max}$. The resulting image amplitude is

$$\psi_i \propto \iint F(\boldsymbol{K})\, M(\boldsymbol{K}) \exp(+2\pi i \boldsymbol{K}\boldsymbol{r})\, d^2\boldsymbol{K}. \qquad (2.12)$$

Multiplication by the masking function $M(\boldsymbol{K})$ in Fourier space results in a convolution with the "point spread function" $M(\boldsymbol{r})$ in direct space. $M(\boldsymbol{r})$ is given by the inverse Fourier transform of $M(\boldsymbol{K})$ as

$$M(\boldsymbol{r}) = J_1(x)/x \quad \text{with} \quad x = (2\pi/\lambda)\alpha_0 \boldsymbol{r}, \qquad (2.13)$$

where J_1 is the first order Bessel function. Equation (2.13) describes the image amplitude of one object point created by the lens with finite aperture α_0. The resulting intensity distribution is $I \propto [J_1(x)/x]^2$, which is the well-known Airy distribution. Equation (2.12) implies that the image of each point is blurred with the point spread function $M(\boldsymbol{r})$ given by (2.13).

Let us turn to a simple example, in which we apply the wave-optical formulation to a crystalline object. We consider an object with amplitude distribution as given in figure 2.11a. This figure shows a two-dimensional section through a colloidal crystal. We use this image to calculate the amplitude distribution in the diffraction plane by Fourier transformation according to equation (2.8). The resulting intensity distribution shows diffraction spots in a sixfold arrangement associated with the sixfold symmetry of the hexagonal close-packed

crystal plane (inset of figure 2.11a). Suppose we want to image the object in figure 2.11a with a lens whose aperture is just large enough to capture the six diffracted beams in the center of the diffraction plane. The lens has no aberrations otherwise. According to equation (2.12), the image produced by this lens is obtained as the inverse Fourier transform of the amplitude distribution in the diffraction plane, masked with the function $M(\boldsymbol{K})$ that selects only the inner six spots. The resulting image intensity distribution is shown in figure 2.11b together with the masked diffracted intensity distribution. The sharp image details are lost, while the particles are still distinguishable. If, however, the six inner spots are not included in the formation of the image, the particles are no longer resolved. This is shown in figure 2.11c, where the masking function has been chosen to exclude the central six spots. These images show that object details are resolved only if the diffracted beams associated with the corresponding spatial frequencies are captured by the objective lens.

Let us now establish a link to the diffraction imaging presented in sections 2.2 and 2.3. We shift the lens diaphragm position to capture one of the diffracted spots (figure 2.11d). Due to the small lens aperture, the particles are still not resolved, but important information about crystal lattice distortions can be obtained. A dark contrast (arrow in figure 2.11d) indicates a region in the crystal, where the lattice is distorted to include a defect, as shown by comparing figs. 2.11a and d. A close look at the corresponding region in figure 2.11a shows that particles are shifted along lattice rows from left to right, resulting in two rows of opposing particles. This distortion extends a few particle diameters into the crystal lattice. Because the distorted region is larger than the crystal lattice constant, it is associated with smaller spatial frequencies. These frequencies are still included in the narrow frequency range captured by the aperture, so that the defect is resolved. To explore the imaging under different diffraction vectors, we shift the diaphragm position to select the lower diffracted spot (figure 2.11e). No contrast is observed. In this case, the corresponding diffraction vector (from the center of the diffraction plane to the selected diffracted beam) is perpendicular to the particle displacements associated with the defect. This shows that lattice distortions are only visible if the particle displacements have a component in the direction of the diffraction vector used for imaging. figures. 2.11d and e illustrate the principal of diffraction contrast imaging to investigate crystal defects.

3. Theory of image contrast

Diffraction contrast encodes important information about crystal lattice distortions. This information can be extracted if the relation between crystal lattice strain and image contrast is known. Theories of diffraction image contrast have been formulated for transmission electron microscopy, and these establish an important link between diffraction contrast and the three-dimensional strain field of crystal defects. Image contrast results from the interference of the transmitted and diffracted beams, which is accounted for in the general dynamical diffraction theory. Kinematical diffraction theory, which considers only the interference of the single scattered beams, represents a simple approach for thin and weakly scattering crystals. This theory provides a good approach for closely refractive-index matched suspensions, which we consider in this review.

In this chapter, we outline the kinematical theory of diffraction image contrast to describe the intensity distribution in laser diffraction images. This needs concepts of lattice planes and the reciprocal lattice, and optical scattering theory. While the diffraction of electrons by atomic crystals is caused by the interaction of the electrons with the periodic atomic potential, the diffraction of light at colloidal crystals results from the periodic modulation of the dielectric constant associated with the periodic arrangement of the particles. The latter is described by Maxwell's equations. Before outlining the kinematical theory of

image contrast, we will address the scattering of light at small spheres in section 3.1, and give a brief introduction into kinematical diffraction theory in section 3.2. Readers familiar with the basic concepts of light scattering and kinematical diffraction should proceed immediately to section 3.3, which describes the kinematical theory of diffraction image contrast. The very short description presented here represents the kinematical theory formulated by Hirsch et al. (1960) for electron microscopy. This theory will be applied to simulate laser diffraction image contrast in chapter 6.

3.1 Scattering of light by small particles

The scattering of light by small particles is a complex topic, and only a few basic ideas can be presented here. There are excellent textbooks (see e.g. van de Hulst 1981 and Bohren and Huffman 1998), to which the reader is referred for further studies. The scattering of light is caused by the interaction of the electromagnetic wave with the particle medium. A treatment of the problem requires the solution of Maxwell's equations with the appropriate boundary conditions. The Maxwell equations formulated in c.g.s. units for a medium with dielectric constant ε, magnetic permeability μ and conductivity σ are:

$$\text{curl}\, \boldsymbol{H} = (4\pi/\text{c})\, \boldsymbol{J} + (1/\text{c})\, \text{d}\boldsymbol{D}/\text{d}t \tag{3.1a}$$

$$\text{curl}\, \boldsymbol{E} = -(1/\text{c})\, \text{d}\boldsymbol{B}/\text{dt} \tag{3.1b}$$

$$\text{div}\, \boldsymbol{D} = 4\pi\, \rho_\text{f} \quad \text{and} \tag{3.1c}$$

$$\text{div}\, \boldsymbol{B} = 0 \tag{3.1d}$$

Here, $\boldsymbol{H}$ and $\boldsymbol{B}$ are the magnetic field and magnetic induction, respectively, $\boldsymbol{E}$ is the electric field, $\boldsymbol{D} = \varepsilon\boldsymbol{E}$ the dielectric displacement, $\boldsymbol{J} = \sigma\boldsymbol{E}$ the current density, ρ_f the density of free charges and c the speed of light. To describe the propagation of waves we write all quantities as complex functions of time in the form

$$A = (a + ib)\, \text{e}^{i\omega t}, \tag{3.2}$$

where the physical quantity represented by A equals the real part of A. With this periodic Ansatz, equations (3.1a) and (3.1b) become

$$\text{curl}\, \boldsymbol{H} = ikn^2\boldsymbol{E} \tag{3.3a}$$

$$\text{curl}\, \boldsymbol{E} = -ik\boldsymbol{H} \tag{3.3b}$$

where

$$k = \omega / c, \tag{3.3c}$$

$$n^2 = \varepsilon - 4\pi i\sigma / \omega, \tag{3.3d}$$

and we have replaced $\boldsymbol{B}$ by $\boldsymbol{H}$, assuming the magnetic permeabiliy $\mu = 1$. Solutions of eqs. (3.3) are plane waves with frequency ω and propagation constant nk described by

$$\psi = \exp[i(n\boldsymbol{kr} + \omega t)], \tag{3.4}$$

where n is the complex refractive index of the medium. We see from equation (3.3d) that for a conducting medium ($\sigma > 0$), the complex refractive index n has a non-vanishing imaginary part, which gives rise to damping of the wave. For the case of a purely dielectric sphere treated here, $\sigma = 0$ and no damping occurs.

We consider a homogeneous dielectric sphere with refractive index n in vacuum. The results that we will obtain can be directly applied to a sphere in a medium with refractive index n_M by simply replacing n with n / n_M. A general solution to this problem was worked out by Mie (1908). This solution, however, is rather formal, and we will not present it within this review. We will focus instead on two limiting cases, namely Rayleigh and Rayleigh-Gans scattering, for which direct analytic solutions exist. In the Rayleigh scattering limit, the particle size is small compared to the wavelength of the incident light, and the particle can be considered to be placed in a homogeneous electric field. Each volume element of the particle is exposed to the same phase of the electric field, and the particle behaves like an oscillating electric dipole, independant of the shape of the particle. The induced dipole moment is

$$\boldsymbol{p} = \alpha \boldsymbol{E_0} \tag{3.5}$$

where $\boldsymbol{E_0}$ is the electric field amplitude of the incident light and α is the polarizability of the particle. The solution of Maxwell's equations for an oscillating dipole shows that at large distances R much larger than the wavelength λ of the electromagnetic radiation, the electric field magnitude of the scattered radiation is given by

$$E_s = -(\omega^2 p \sin\chi) / (c^2 R) \tag{3.6}$$

where ω is the frequency of the oscillating dipole, p the induced dipole moment and χ is the angle between the direction of the dipole and the direction of the scattered electromagnetic radiation. Since the intensity is given by $I = (c / 8\pi) E^2$, the scattered intensity emitted by the dipole is

$$I_s = (c / 8\pi) (\omega^4 p^2 \sin^2\chi / (c^4 R^2), \tag{3.7}$$

which shows the famous fourth power dependence of the intensity on ω (Lord Rayleigh, 1871a,b). This frequency dependence accounts for the blue color of the sky, since molecules in the atmosphere scatter the blue part of the solar spectrum with greater intensity than the lower frequency red components. For our dielectric particle, the dipolemoment $\boldsymbol{p}$ is given by the integral

$$\boldsymbol{p} = \int \boldsymbol{P} \, \mathrm{d}V, \tag{3.8}$$

where the polarization $\boldsymbol{P}$ can be expressed in terms of the refractive index n of the particle as

$$\boldsymbol{P} = (n^2\text{-}1) (\boldsymbol{E} / 4\pi) \tag{3.9}$$

(Jackson 1999). Generally, the electric field in equation (3.9) in turn depends on the polarization of the particle, which complicates the problem. For particles with refractive index close to that of the surrounding medium ($n = 1$), $\boldsymbol{E}$ can be replaced by the applied field $\boldsymbol{E_0}$ so that the dipole moment

$$\boldsymbol{p} = [(n^2\text{-}1) / 4\pi] V_p \boldsymbol{E_0}, \tag{3.10}$$

where V_p is the particle volume. Hence, in this limit, the polarizability of the particle is simply

$$\alpha = [(n^2\text{-}1) / 4\pi] V_p. \tag{3.11}$$

If the refractive index of the particle is not close to that of the surrounding medium, the problem can still be solved for specific particle shapes. Lorentz has shown that for spherical particles with radius a the polarizability of the particle is given by

$$\alpha_s = [(n^2 - 1) / (n^2 + 2)] a^3. \tag{3.12}$$

The Rayleigh scattering limit considered so far applies only if the phase of the electromagnetic wave does not change appreciably across the particle. For particles with sizes of the order of the wavelength of light, this condition is not fullfilled. For such particles, however, another limit exists: if the phase shift between the wave inside the particle and that outside is small, then the scattering of light can be understood as simultaneous Rayleigh scattering by all volume elements of the sphere. This limit is known as Rayleigh-Gans scattering (Lord Rayleigh 1881, Gans 1925). The condition is fullfilled for particles with refractive index close to one. Scattering at sphere volume elements separated by $\boldsymbol{r}$ cause the phase difference

$$\Delta\varphi = 2\pi \boldsymbol{r} \boldsymbol{K}, \tag{3.13}$$

where the diffraction vector $\boldsymbol{K} = \boldsymbol{k} - \boldsymbol{k_0}$ as defined in (2.6). This phase difference leads to attenuation of the scattered intensity due to the interference of the scattered beams. The resulting electric field amplitude of the scattered light is obtained by summing the contributions from all volume elements of the sphere, taking into account the relative phases of the waves. For a homogeneous particle, we obtain the resulting scattered intensity

$$I_s(\theta) = |(1/V) \int \mathrm{e}^{2\pi i \Delta\varphi} dV|^2 I_s(\theta = 0). \tag{3.14}$$

We define the particle form factor

$$f(\boldsymbol{K}) = (1/V) \int \mathrm{e}^{2\pi i \Delta\varphi} dV, \tag{3.15}$$

which contains the dependence of the scattered intensity on the particle size and shape. The intensity at forward scattering $I_s(\theta = 0)$ equals the intensity in the Rayleigh scattering limit,

equation (3.7). The integral in (3.15) can be evaluated for various particle shapes. For spheres, one obtains

$$f(u) = (3/u^3)\,(\sin u - u\cos u), \qquad (3.16)$$

where $u = 2\,ka\sin(\theta/2)$. (3.16) represents the form factor of spherical particles in the Raleigh-Gans scattering limit. It can be employed to calculate diffracted beam intensities of crystals composed of dielectric particles in the appropriate limits.

3.2 Diffraction from colloidal crystals

In this section, we present a brief overview over the diffraction of light at colloidal crystals. We can only touch on a few basic concepts here: Our focus will be on the kinematical diffraction theory, which is presented in the first paragraph, and we will discuss the applicability of dynamical theory in the second paragraph. The third paragraph discusses diffraction at real crystals, the occurence of diffuse scattering, and Kossel lines that are observed in close analogy to x-ray and electron scattering of atomic crystals.

3.2.1 Kinematical diffraction theory

We consider a crystal unit cell that contains particles i with form factors f_i. The particles are placed at positions $\boldsymbol{v}_i$ with respect to the origin of the unit cell. We define the structure factor F_m that describes the scattering of light at the arrangement of particles in the unit cell by

$$F_m = \sum_i f_i\, e^{-2\pi i \boldsymbol{K}\boldsymbol{v}_i}, \qquad (3.17)$$

where the exponential function takes into account the relative phase of the waves scattered at the particles. We construct a perfect crystal lattice by periodic translation of the unit cell to the lattice positions

$$\boldsymbol{r}_m = m_1\,\boldsymbol{a_1} + m_2\,\boldsymbol{a_2} + m_3\,\boldsymbol{a_3}, \qquad (3.18)$$

where $\boldsymbol{a_1}$, ..., $\boldsymbol{a_3}$ are the basis vectors spanning the crystal lattice, and m_1, ..., m_3 are integer numbers. The resulting periodic arrangement of particles produces diffracted radiation with the amplitude

$$\psi = \sum_m F_m\, e^{-2\pi i \boldsymbol{K}\boldsymbol{r}_m}, \qquad (3.19)$$

where F_m describes the scattered amplitude from each unit cell, and the exponential accounts for the relative phases of the waves scattered at the unit cells. Strong diffraction occurs if the three Laue conditions

$$\boldsymbol{K}\boldsymbol{a_1} = h;\;\; \boldsymbol{K}\boldsymbol{a_2} = k;\;\; \boldsymbol{K}\boldsymbol{a_3} = l \qquad (3.20)$$

where h, k, and l are integers are fulfilled. This corresponds to the Bragg reflection from crystal planes with Miller indices h, k, and l. Condition (3.20) is fulfilled if $\boldsymbol{K}$ equals a vector of the reciprocal lattice, described by

$$\boldsymbol{g}_{hkl} \equiv h\boldsymbol{a_1}^* + k\boldsymbol{a_2}^* + l\boldsymbol{a_3}^* \qquad (3.21)$$

with the basis vectors of the reciprocal lattice

$$\boldsymbol{a_i}^*\boldsymbol{a_j} = \delta_{ij}. \qquad (3.22)$$

In this case, constructive interference occurs and the scattered amplitude from all unit cells add up to the total scattered amplitude

$$\psi_g = \sum_m F_m \qquad (3.23)$$

This amplitude is only determined by the structure factor of the unit cell, which vanishes if the scattered waves from all atoms in the unit cell cancel each other. In this case, a reciprocal lattice vector is not associated with a Bragg reflection. Therefore, while the position of the reflections is given by the reciprocal lattice construction (3.21), their relative intensities are determined by the structure factor (3.17). We will evaluate the structure factor for the fcc lattice here, as we will be concerned with fcc colloidal crystals later in this review. We choose

the origin of the coordinate system at the center of the unit cell so that the sine terms in (3.17) cancel due to symmetry reasons. Hence, the structure factor can be written as

$$F_{hkl} = \sum_i f_i \cos\left[2\pi\left(h\nu_{i,1} + k\nu_{i,2} + l\nu_{i,3}\right)\right]. \tag{3.24}$$

Four atoms are located at (0,0,0), (1/2,1/2,0), (1/2,0,1/2), and (0,1/2,1/2), so that

$$F_{hkl} = f\,(1 + \cos\pi(h+k) + \cos\pi(h+l) + \cos\pi(k+l)) \tag{3.25}$$

We can easily see that

$$F_{hkl} = 4f \quad \text{for } h, k \text{ and } l \text{ all even or all odd} \tag{3.26a}$$

and

$$F_{hkl} = 0 \quad \text{otherwise.} \tag{3.26b}$$

Hence, a reflection does only occur if h, k, and l are either all even or all odd. This indicates that the reciprocal lattice of fcc is bcc. The form factor f is given by (3.16) for small, weakly scattering colloidal particles in the Rayleigh-Gans limit.

Infinitely sharp diffraction spots are obtained for infinite crystal lattices only. For crystals of finite size, the diffraction peaks broaden, and diffraction takes place over a range of angles around the Bragg angle. To determine the diffracted beam intensity as a function of deviation from the Bragg angle, we write

$$\boldsymbol{K} = \boldsymbol{g}_{hkl} + \boldsymbol{s}, \tag{3.27}$$

where $\boldsymbol{s}$ represents a small deviation from the reciprocal lattice vector. We substitute (3.27) into (3.19) to obtain

$$\psi_g = \sum_m F\, e^{2\pi i \boldsymbol{s}\boldsymbol{r}_m}, \tag{3.28}$$

where we have used the identity (3.22) for the reciprocal lattice vector $\boldsymbol{g}_{hkl}$. Approximation of the sum by an integral yields

$$\psi_g \propto \int e^{-2\pi i \boldsymbol{s}\boldsymbol{r}}\, dV, \tag{3.29}$$

which is the Fourier transform of the shape of the crystal. Therefore, each reciprocal lattice point is convoluted with the Fourier transform of the crystal shape. We can easily evaluate (3.29) for a rectangular crystal with dimensions U, W and T along the x, y, and z directions, respectively. We obtain

$$|\psi_{\boldsymbol{g}}| \propto [\sin(\pi U s_x)/(\pi s_x)]\,[\sin(\pi W s_y)/(\pi s_y)]\,[\sin(\pi T s_z)/(\pi s_z)] \tag{3.30}$$

where s_x, s_y and s_z are the components of $\boldsymbol{s}$ along the x, y, z directions. The intensity $I = \psi_{\boldsymbol{g}}\psi_{\boldsymbol{g}}^*$ is plotted as a function of s_z in figure 3.1. The central maximum of the intensity curve has a width at half maximum proportional to $1/T$. This dependence of the peak width on the crystal size has been exploited to determine the size of colloidal crystals by light scattering. Time resolved measurements of the width of Bragg reflections have been used to monitor the average crystal size as a function of time in crystallizing colloidal suspensions (Dhont *et al.* 1992, Harland *et al.* 1995, Palberg 1999, Wette *et al.* 2003). As the crystals nucleate and

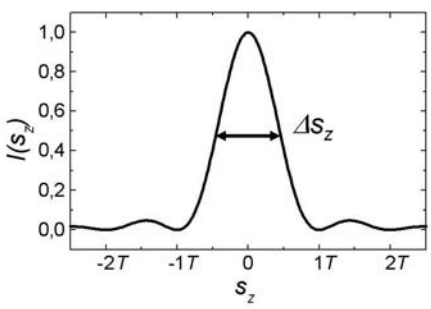

Figure 3.1 Intensity distribution as a function of excitation error around a Bragg reflection. The half peak width Δs_z is proportional to the inverse sample thickness, T^{-1}.

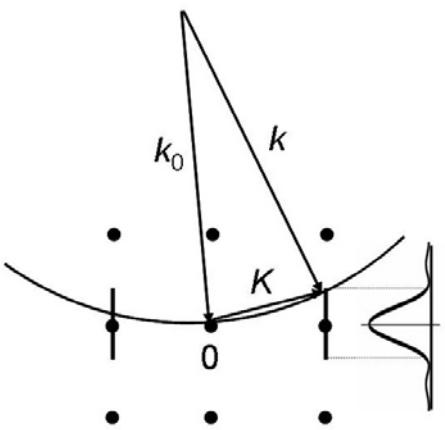

Figure 3.2 Reflected beam construction for a thin crystal plate
The schematic shows the wave vectors of the incident and diffracted beams, $\boldsymbol{k}_0$ and $\boldsymbol{k}$, the diffraction vector $\boldsymbol{K} = \boldsymbol{k} - \boldsymbol{k}_0$, and the intensity distribution in the form of a spike for a thin crystal plate oriented normal to the incident beam. Diffraction occurs in directions, where a sphere of radius $|\boldsymbol{k}_0|$ through the origin intersects the spikes (Ewald sphere construction).

grow, the Bragg peaks are observed to sharpen. While the average crystal size is determined from the width of the crystal structure factor, the area under the crystal peak yields the relative amount of crystal phase in the crystal-liquid mixture (Harland *et al.* 1995). Combined with the average crystal size, this allows determination of the number density of growing crystals. These measurements have been used to determine bulk nucleation rates, which can be directly compared with predictions from classical nucleation theory. Reasonable agreement is observed (Harland *et al.* 1995, Auer and Frenkel 2001, Wette *et al.* 2003).

Within this review, we will be concerned with crystals in the form of thin plates. Such crystals are obtained by sedimentation of the particles onto a template (van Blaaderen *et al.* 1997, Hoogenboom *et al.* 2004). The limited extension of the crystals in the direction perpendicular to the template results in diffraction peak intensities that are spread out in the form of spikes normal to the crystal plate. A schematic picture illustrates a two-dimensional section through the reciprocal space of such a crystal in figure 3.2. Diffracted beams are obtained by determining the intersections of a sphere of radius $k_0 = 1/\lambda$ through the origin of the reciprocal lattice with the reciprocal lattice points (Ewald construction). Due to the confinement of the crystal in the z-direction, the reciprocal lattice points are elongated in the z-direction of the reciprocal space. As a result, the Ewald sphere intersects many reciprocal lattice points, meaning that many reflections are visible simultaneously. For thin crystal plates, the deviation parameter $\boldsymbol{s}$ is always nearly parallel to the normal of the plate, and we can write

$$\boldsymbol{s} = (0,0,s_z). \tag{3.31}$$

The parameter $s = s_z$ is called the excitation error, and is an important parameter that determines diffraction image contrast.

3.2.2 Dynamical diffraction

The kinematical theory treated in the preceeding paragraph is valid only if the diffracted wave exhibits no further scattering. This is a good approximation for thin and weakly scattering samples. If the diffracted amplitude becomes large, however, the diffracted wave itself is scattered by the crystal. The more general dynamical diffraction theory describes this interaction of the incident and diffracted beams and includes multiple scattering. Dynamical

diffraction theory has been originally formulated for x-rays (Darwin 1914) and later for electrons (Howie and Whelan 1961, 1962) and is treated in standard textbooks of x-ray and electron diffraction (Zachariasen 1945, Pinsker 1978, Hirsch *et al.* 1965). This theory is used to account for the relative intensities of the diffracted and transmitted beams. In addition, it predicts a slight shift of the reflection positions with respect to the positions predicted by kinematical theory. Dynamical diffraction theory has been applied to strongly scattering colloidal crystals by adapting the theory formulated for x-rays (Flaugh *et al.* 1984, Spry and Kosan 1986). In their pioneering work Flaugh *et al.* (1984) used crystals of polystyrene particles in water to build optical filters. They found that due to the large refractive index mismatch between the particles and water, a crystal thickness of 50 layers is enough to diffract essentially all incident light that satisfies the Bragg condition. Dynamical x-ray diffraction theory (Zachariasen 1945) together with optical scattering theory (van de Hulst 1981) is able to account for the observed diffraction of light (Spry and Kosan 1986, Rundquist *et al.* 1989). The theory describes the relative intensities of the diffraction maxima and their shift from the Bragg positions observed in light scattering experiments.

Crystals with strong diffraction of light have important applications as light switches in photonic devices. Strong scattering by the constituent units is essential for the functionality of these devices. This is achieved by using materials with very strong contrast i.e. large ratio of refractive indices. Full bandstructure theory is needed to describe the interaction of light with these materials (Markos and Soukoulis 2008, Joannopoulos *et al.* 2008). Recent developments include the fabrication of inverse structures that consist of holes in a solid matrix to obtain a real bandgap of photonic states. For the scope of this review we will focus on the opposite case of weakly scattering crystals, achieved by matching the refractive index of the suspending liquid with that of the constituent particles. Simple kinematical theory is applied to describe the diffraction of light at these crystals.

3.2.3 Diffraction patterns

Diffraction patterns can be used to determine the complete set of reciprocal lattice vectors of colloidal crystals (Rogers and Lagerlöf 2008a). In general, these patterns show a diffuse background superimposed onto the sharp diffraction spots expected for the perfect crystal lattice. Irregularities in real crystals alter the perfect lattice interference condition, and cause broadening of the diffraction peaks as well as scattering of light in between the peaks of the perfect lattice. In analogy with x-ray and electron diffraction, the diffusely scattered intensity can be decomposed into coherently and incoherently scattered intensities (Rundquist *et al.* 1991). Coherent scattering arises from defects that alter the lattice periodicity locally. Incoherent diffuse scattering arises from the collective motions of the particles associated with lattice phonons. Both parts, the coherent and incoherent scattering, have been observed in diffraction patterns of colloidal crystals (Clark *et al.* 1979, Rundquist *et al.* 1991). Colloidal crystals exhibit thermally excited lattice vibrations (Cheng *et al.* 2000, Reinke *et al.* 2007), which cause a distortion of the lattice periodicity that has two major effects: it leads to a decrease of the diffracted intensity by the Debye Waller factor, e^{-2M}, and to thermal diffuse scattering between and near the Bragg reflections (Zachariasen 1945, Reimer 1993). Thermal diffuse scattering is described by the interaction of light with phonons of momentum ($hq/2\pi$) and energy ($h\omega/2\pi$), where q and ω are the phonon wave vector and frequency. The exchange of momentum between the light and phonons leads to the altered Bragg condition

$$\boldsymbol{K} = \boldsymbol{g}_{hkl} + \boldsymbol{q}. \qquad (3.32)$$

Typically, the magnitude of $\boldsymbol{q}$ is much smaller than that of $\boldsymbol{K}$, so that the corresponding light is scattered in directions close to the Bragg angles of the perfect, rigid lattice. Light scattering measurements performed near Bragg peaks have elucidated this intensity distribution

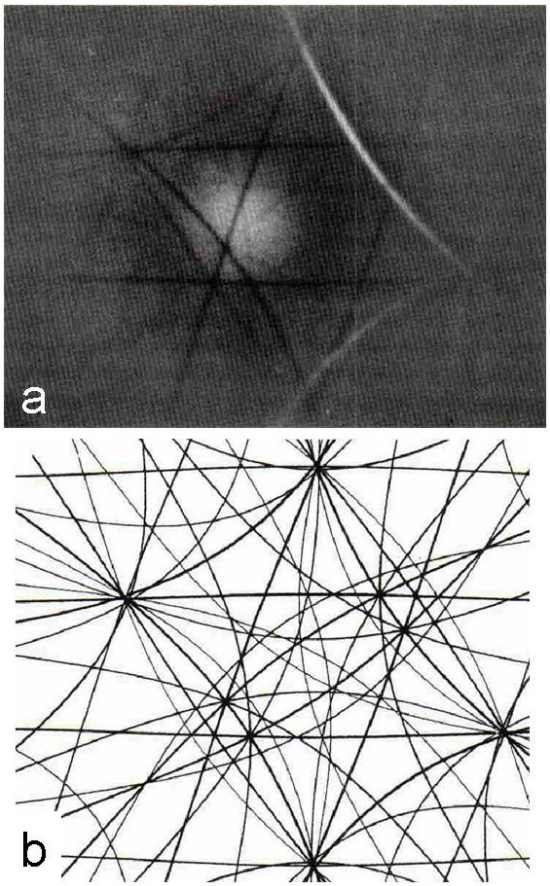

Figure 3.3 Kossel lines of bcc colloidal crystals
(a) Photograph of Kossel lines of bcc crystals oriented with the (110) planes parallel to the plane of observation. (b) Corresponding computer generated diagram (Pieranski 1983).

experimentally. Rundquist *et al.* (1991) used the measured intensity distribution to determine phonon velocities in colloidal crystals. The characteristic fluctuation time associated with the diffusely scattered intensity can be conveniently identified with light scattering (Clark *et al.* 1979).

In close analogy to x-ray and electron diffraction, the diffusely scattered background contains a pattern of lines, also known as Kossel or Kikuchi lines (Kikuchi 1928) (figure 3.3). These lines arise from Bragg scattering of the diffusely scattered light: All rays that are incident under the Bragg angle θ_B to a set of lattice planes are diffracted. These rays lie on a cone with angle 90°-θ_B coaxial with the normal to the lattice planes, the so-called "Kossel cones". Intersection of these Kossel cones with the plane of observation results in Kossel lines. Because the Kossel cones are fixed with the reciprocal lattice of the crystal, Kossel lines move thoroughly fixed with the crystal as the crystal is rotated, in contrast to Bragg reflections, which merely change their relative intensities. Hence, Kossel diagrams provide a convenient way to determine crystal orientations. In electron microsopy, Kossel lines serves as an important guide through the reciprocal space of the crystal. They provide a 'map' that allows changing the orientation of the crystal along specific crystal lattice planes. In principle, each Kossel diagram allows reconstruction of the entire reciprocal lattice of the crystal. For x-ray and electron diffraction, however, only a small portion of the Kossel diagram is available at once because of the short wavelength of the radiation compared to the crystal lattice constant. Colloidal crystals, in contrast, allow access to large portions of the Kossel diagram, because the wave length of light is of the same order as the crystal lattice constant. Pieranski

et al. (1981) have shown that half of the Kossel diagram or even the full Kossel diagram can be obtained when using a spherical screen around the diffracting colloidal crystal. These authors have used Kossel diagrams to determine the structure, orientation, and density of colloidal crystals from simple light diffraction experiments. Recently, divergent beam techniques have been applied to determine lattice parameters with an accuracy of 1% and lattice orientations with an accuracy of 2° (Rogers and Lagerlöf 2008b).

3.3 Kinematical theory of image contrast

Diffraction image contrast occurs when radiation diffracted at a crystal is projected to produce a real-space image of the crystal. Theories of diffraction image contrast have been formulated for electron diffraction, and they have played a central role for the interpretation of image contrast in conventional transmission electron microscopy. These theories account for the contrast produced by dislocations and other crystal defects as they provide an important link between image contrast and the strain introduced by these defects.

In this chapter, we will present the kinematical theory of electron diffraction image contrast following the treatment by Hirsch *et al.* 1960. While this simple treatment accounts for basic features of the diffraction contrast such as the visibility of defects and their contrast width, dynamical diffraction theory is used to account for the intensity distribution more quantitatively (Howie and Whelan 1962). We will focus on image contrast obtained when the crystal is close to Bragg orientation so that only one diffracted beam is visible. In this orientation, diffraction occurs at *one particular* set of lattice planes, and the resulting diffraction contrast can be interpreted most easily.

To calculate diffraction image contrast, it is necessary to work out the intensity distribution at the exit surface of the crystal. This intensity distribution will then be imaged by lenses. We will apply this treatment to perfect crystals in section 3.3.1 and to crystals containing dislocations in section 3.3.2.

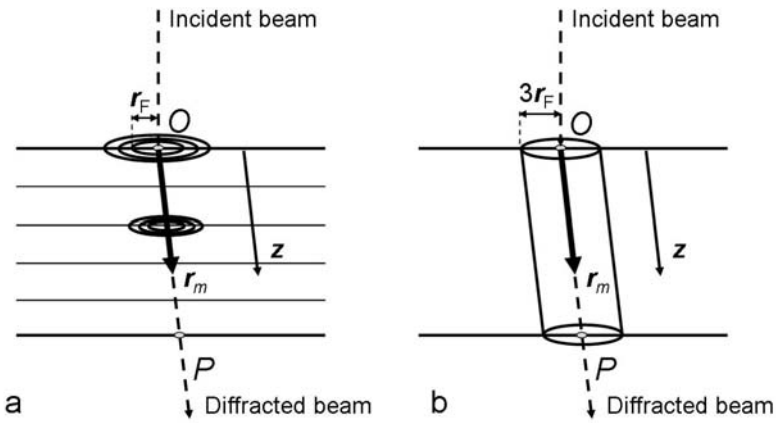

Figure 3.4 Column approximation for the image intensity at point *P* at the crystal exit surface
Shown are schematic cross sections through the crystal plate, and incident and diffracted beam directions. (a) Fresnel zone construction for the diffracted beam intensity at *P*. r_F indicates the radius of the first Fresnel zone. (b) Crystal column used to calculate the diffracted beam intensity at *P*. The column is parallel to the diffracted beam direction and is paramatrized by r_m and z.

3.3.1 Diffraction contrast images of perfect crystals

Image of the Diffracted Beam

To calculate the amplitude of the diffracted beam at a point P at the bottom surface of the crystal, the crystal is splitted into layers parallel to the surface (figure 3.4a). Most of the contribution from each plane to the amplitude at P comes from the first few Fresnel zones, an area with radius roughly $3r_F$, where

$$r_F = \sqrt{\lambda D_F} \tag{3.33}$$

is the radius of the first Fresnel zone. Here, D_F is the distance from the center of the Fresnel zone to P. This area is largest for layers at the top surface of the crystal, i.e. for $D_F \approx T$, the thickness of the crystal film. For atomic crystals, $r_F \sim 6$Å for a typical crystal thickness of 1000 Å, while for colloidal crystals, $r_F \sim 5\mu$m for a crystal thickness of 40 μm and $\lambda = 632$ nm. These results indicate that most of the contribution to the amplitude at P comes from a narrow column with diameter of a few particle diameters, whose axis is parallel to the diffracted beam. The resulting diffracted beam amplitude at point P is obtained by adding the contributions from all points along the column taking into account the relative phases of the waves. Hence, the amplitude

$$A \propto \sum_m e^{-2\pi i \boldsymbol{K}\boldsymbol{r}_m}\ , \tag{3.34}$$

where $\boldsymbol{r}_m$ are the vectors from the origin to all points m along the column (figure 3.4b). We substitute $\boldsymbol{K} = \boldsymbol{g} + \boldsymbol{s}$, where $\boldsymbol{s}$ is a small deviation from the reciprocal lattice vector $\boldsymbol{g}$. For a thin crystal plate with normal along the z-axis, $\boldsymbol{s}$ is parallel to the z-direction, and can be replaced according to (3.31). We further replace the sum in (3.34) by an integral and obtain for the amplitude at P

$$A \propto \int_0^T e^{-2\pi i sz}\, dz\ , \tag{3.35}$$

which after evaluation of the integral becomes

$$A \propto \left[\sin(\pi Ts)/(\pi s)\right] e^{-\pi i Ts}\ . \tag{3.36}$$

The intensity is $I \propto \sin^2(\pi Ts)/(\pi s)^2$, which is an oscillating function of the sample thickness. This gives rise to thickness contours for non-planar specimens. The periodicity of these oscillations is $\Delta z = s^{-1}$ and can, for known excitation error, be used to determine thickness differences of the crystal film.

It is instructive to illustrate the integral (3.35) in an amplitude-phase diagram (figure 3.5). The amplitude-phase diagram of all contributions $e^{-2\pi i sz}\, dz$ of the column is a circle of radius $(1/2\pi s)$. The resulting amplitude A is given by the vector OP. As the thickness increases, P moves along the circle, and the amplitude oscillates with the thickness just as predicted by (3.36). As the crystal orientation is changed for a given thickness, s and therefore the radius of the circle in figure 3.5 changes. This gives rise to bend contours in buckled specimens.

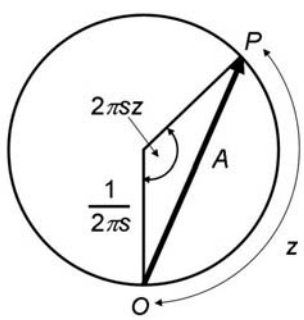

Figure 3.5 Amplitude-phase diagram for a column in a perfect crystal. The resultant amplitude A equals the length of the vector from O to P.

Image of the transmitted beam

In the kinematical approximation, the intensities I_d and I_t of the diffracted and transmitted beams add up to give the total intensity I_0 of the incident radiation. Hence, the transmitted beam intensity

$$I_t = I_0 - I_d. \tag{3.37}$$

This means that the images of the transmitted and diffracted beams are complementary.

3.3.2 Diffraction contrast produced by dislocations

A crystal defect introduces atomic displacements $\Delta \boldsymbol{r}_n$ from the ideal positions $\boldsymbol{r}_n$ of the perfect lattice. These displacements lead to an additional phase in the exponential in (3.35) given by

$$\varphi = 2\pi \boldsymbol{K} \Delta \boldsymbol{r}_n, \tag{3.38}$$

This additional phase changes the interference of waves produced by the elements of the column and therefore alters the resulting local amplitude. To determine the effect of this additional phase on the image amplitude, we substitute $\boldsymbol{K} = \boldsymbol{g} + \boldsymbol{s}$ to obtain

$$\varphi = 2\pi \boldsymbol{g}\, \Delta \boldsymbol{r}_n, \tag{3.39}$$

where we have neglected terms in second order of small quantities. We evaluate the integral (3.35) with the additional phase (3.39) for a screw dislocation here. We consider a long, straight screw dislocation at depth z_0 parallel to the crystal surface (figure 3.6). The displacement field associated with this screw dislocation is (see e.g. Hirth and Lothe 1982)

$$\Delta \boldsymbol{r} = \boldsymbol{b}\,(\Theta / 2\pi) = (\boldsymbol{b} / 2\pi) \tan^{-1}[(z-z_0)/y], \tag{3.40}$$

where $\boldsymbol{b}$ is the Burgers vector of the dislocation and y is the lateral distance from the dislocation line. This displacement field gives rise to the additional phase angle

$$\varphi = \boldsymbol{g} \cdot \boldsymbol{b} \tan^{-1}[(z - z_0) / y]. \tag{3.41}$$

No change in phase occurs for $\boldsymbol{g} \cdot \boldsymbol{b} = 0$, i.e. when the Burgers vector of the dislocation is perpendicular to the reciprocal lattice vector used for imaging. In this case, the atomic displacements have no component parallel to the reciprocal lattice vector and the dislocation is not visible. The invisibility condition $\boldsymbol{g} \cdot \boldsymbol{b} = 0$ for dislocations allows determination of their Burgers vector directions: if $\boldsymbol{g}_1$ and $\boldsymbol{g}_2$ are two linear independant diffraction vectors, for which the dislocation is invisible, then the Burgers vector is parallel to the cross product $\boldsymbol{g}_1 \times \boldsymbol{g}_2$. The determination of Burgers vector directions is an important application of the invisibility condition. It is employed to investigate dislocation arrays in various crystalline materials by transmission electron microscopy (Williams and Carter 1996).

For $\boldsymbol{g} \cdot \boldsymbol{b} \neq 0$, the phase φ in (3.41) does not vanish, and adds to the phase in the exponential in (3.35). In this case, the dislocation produces a contrast. Substitution of (3.41) into (3.35) yields the amplitude

$$A' \propto \int_0^T \exp\left\{-i\boldsymbol{g} \cdot \boldsymbol{b} \tan^{-1}\left[(z - z_0)/y\right]\right\} \exp(-2\pi i\, sz)\, dz\,. \tag{3.42}$$

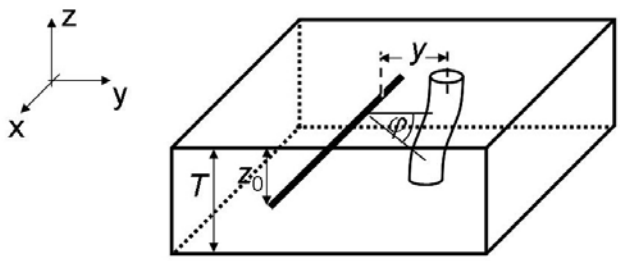

Figure 3.6 Column approximation for a crystal plate containing a screw dislocation
The schematic shows the distorted crystal column at lateral distance y to the dislocation line (thick solid line). The dislocation lies at depth z_0 below the crystal surface.

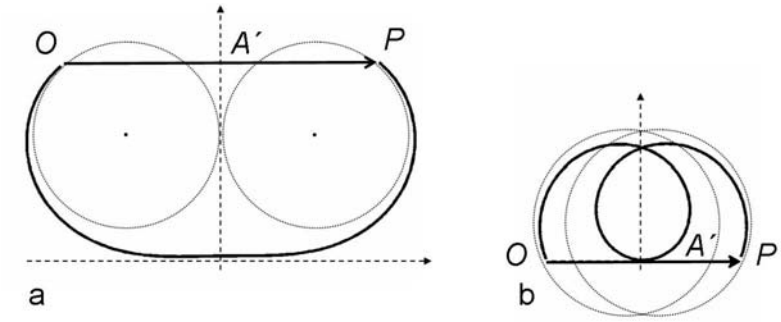

Figure 3.7 Amplitude-phase diagrams for columns close to a screw dislocation for $\boldsymbol{g}\cdot\boldsymbol{b}$ = 1 and $2\pi sy$ = -0.8 (a) and for $\boldsymbol{g}\cdot\boldsymbol{b}$ = 1 and $2\pi sy$ = +0.8 (b). Diagrams in (a) and (b) correspond to opposite sides of the dislocation line. The amplitude A is larger for one side of the dislocation (a) than for the other side (b).

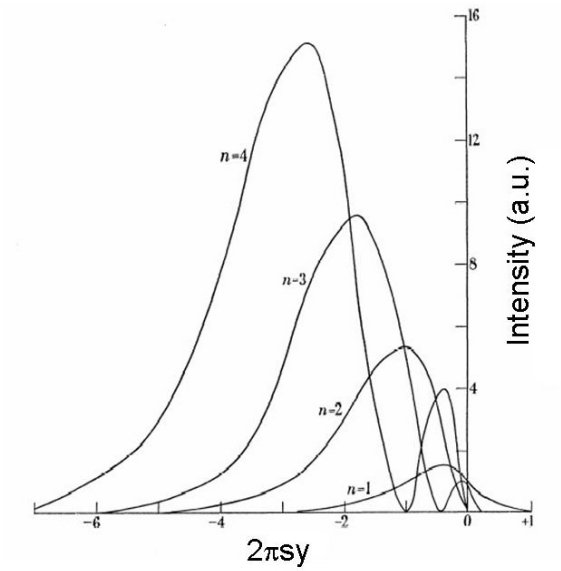

Figure 3.8 Intensity profile across a screw dislocation
The curves show diffracted intensities for several values of $n=\boldsymbol{g}\cdot\boldsymbol{b}$ as a function of $2\pi sy$, where y is the distance from the dislocation line and s is the excitation error (Hirsch *et al.* 1960).

We evaluate this integral by considering the corresponding amplitude-phase diagram in figure 3.7. The additional phase leads to unwinding or upwinding of the circular amplitude-phase graph of the perfect crystal. Largest deviations occur for z near z_0, where the displacement magnitudes are largest. For a point on the right side of the dislocation line ($y > 0$), the additional phase angle subtracts from the phase $2\pi i\, sz$ of the perfect crystal resulting in an unwinding of the spiral (figure 3.7a). This leads to an amplitude A' larger than that of the perfect crystal meaning that the crystal is turned effectively into a reflecting position on this side of the dislocation. On the contrary, little changes of the resulting amplitude occur for a point on the left side of the dislocation line ($y < 0$). On this side, the phase angle adds to the phase of the perfect crystal and the spiral winds up (figure 3.7b). On this side of the dislocation, the crystal is turned away from the reflecting position. Hence, strong contrast is expected on one side of the dislocation only. This is illustrated by plotting the image intensity $I \propto A'^2$ as a function of y for points P across the dislocation line in figure 3.8.

4. Laser Diffraction Microscopy of dislocations in colloidal single crystals

Dislocations in colloidal crystals produce optical diffraction contrast. Laser diffraction microscopy uses coherent laser light to explore the diffraction imaging of dislocations under well-defined conditions. These images serve two main goals: They give an overview over the defect arrangements to elucidate defect mechanisms on intermediate lengths scales. Second, the visibility of defects, and their contrast profile offer insight into the strain field of dislocations and their topology. In this chapter, we will review the application of laser diffraction microscopy to study dislocations in colloidal crystal films. Single crystal films of high structural perfection are obtained by slow sedimentation of colloidal particles onto a template, in analogy to the epitaxial growth of atomic crystal films. These films offer model systems to study the propagation of dislocations in these soft crystals. Stretched templates are used to induce a uniform strain that results in a regular array of dislocations accommodating the misfit between the crystal and template lattice constants. Indentation is used to induce a strongly inhomogeneous strain distribution that drives the nucleation of individual dislocations. Laser diffraction microscopy provides images of the dislocation arrangements and their propagation. We show that continuum models offer a valuable description of the observed dislocation propagation.

4.1 Colloidal single crystals

To study the intrinsic properties of dislocations without the influence of grain boundaries or other defects, care should be taken to obtain large single crystals of high structural perfection. Several methods are known to achieve large colloidal crystals, including slow sedimentation of colloidal particles on a patterned substrate (van Blaaderen *et al.*, 1997), controlled nucleation and growth using a temperature gradient (Cheng *et al.* 1999), and controlled, gentle shear of a crystallizing suspension (Clark *et al.*, 1979, Haw *et al.* 1998). Hard-sphere colloidal particles form hexagonal close-packed layers that are stacked randomly. These can be considered as fcc or hcp crystals with a high density of stacking faults along the hexagonal close-packed plane. The use of a template, however, enables the growth of pure fcc (van Blaaderen *et al.* 1997) and hcp (Hoogenboom *et al.* 2004) crystals. This template, which fixes the positions of the particles in the first layer, determines the stacking sequence of the hexagonal close-packed planes. Crystals with a high degree of perfection are obtained when a very dilute colloidal suspension is used, so that the sedimentation of particles occurs at a very low rate. This colloidal crystal growth technique is analogous to the epitaxial growth of atomic crystalline films.

We focus here on fcc crystals grown in the <100> direction. In this direction, the stacking deposition alternates between only *two* sets of positions A and B and there is no stacking degeneracy. Monodisperse silica particles are sedimented onto a template that consists of particle-size holes in an fcc {100} arrangement. Almost defect-free crystals are obtained when the template lattice constant matches the equilibrium interparticle separation of the colloidal crystal (van Blaaderen *et al.* 1997, Schall *et al.* 2004). The particles used here have a diameter of $2a = 1.55\,\mu\text{m}$ and a polydispersity of less than 3.5%. Perfect crystals are obtained on templates with lattice constant $a_0 = 1.63\,\mu\text{m}$, which is slightly larger than the particle diameter, reflecting the slight particle charge. Crystals grown on templates with slightly larger or smaller lattice constant show a high density of defects (Schall *et al.* 2004, Hoogenboom *et al.* 2004). These defects accommodate the misfit between the crystal and template lattice constants in close analogy to misfit dislocations in atomic crystal films that are grown on substrates with slightly different lattice constant (Hull and Bean 1992). The lattice mismatch introduces a uniform strain in the crystal film that drives the formation of

these defects. In the example presented here, colloidal crystals are grown on a template with lattice constant about 1.65 μm instead of the ideal one of 1.63 μm resulting in a uniform strain of $\varepsilon_0 = 1.5\%$.

4.2 Imaging of dislocations

LDM images provide an excellent overview over the formation of defects in the strained crystal films. The images of the strained films look similar to those of unstrained films (figure 2.5b and c) until a film thickness of 22 μm, but develop a high density of lines for crystals thicker than 31 μm (figure 4.1). The appearence of these lines indicates that dislocations nucleate and grow in the crystal film. Each dislocation marks the boundary of a surface, where one part of the crystal has been uniformly translated with respect to the other. This translation accommodates the misfit between the crystal and substrate lattice constants. The translation vector equals the Burgers vector of the dislocation. LDM is able to determine the direction of the Burgers vector by evaluating the visibility of dislocations. We explore this visibility by choosing different diffracted beams for imaging. The diffraction vector used for imaging in figure 4.1a lies along the [110] direction (see inset of figure 4.1a). If we instead choose a diffraction vector along [1-10] perpendicular to [110], a set of perpendicular lines appears, which indicate an array of dislocations with perpendicular line direction (figure 4.1c and d). Since the crystal film is stretched in both spatial directions, both dislocation line directions are in fact expected. One set of dislocations is, however, invisible in each image, because the Burgers vector of these dislocations is perpendicular to the diffraction vector used for imaging. By comparing figures. 4.1a and c we conclude that the Burgers vector is always perpendicular to the imaged dislocation lines. Hence, the dislocations are of edge type.

Determination of the full Burgers vector direction would require another linear independant diffraction vector for which the dislocations are invisible. The Burgers vector direction is then obtained from the cross product of both linearly independant diffraction

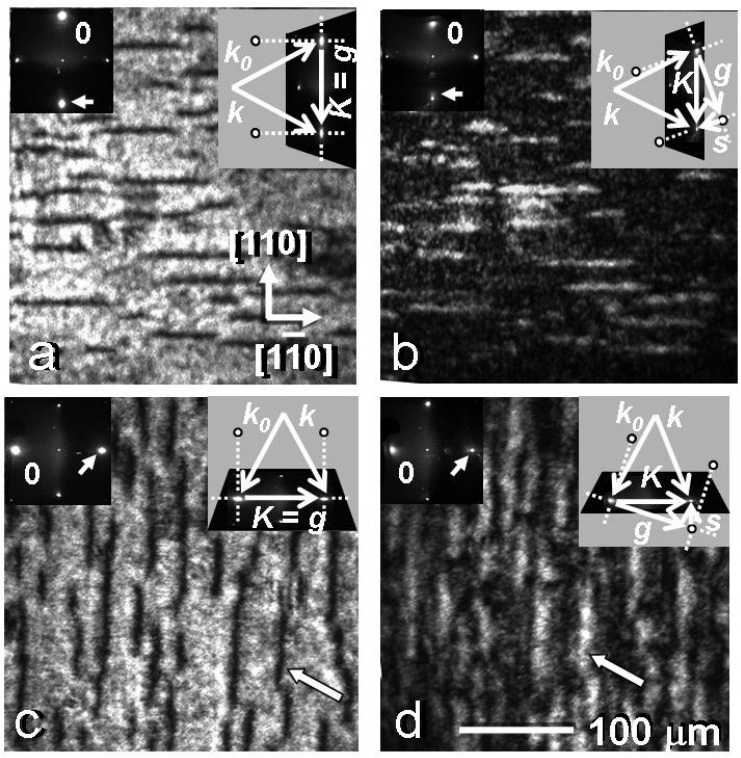

Figure 4.1 Laser diffraction microscope images of dislocations in strained colloidal crystal films
The upper left inset shows the diffraction pattern, where 0 indicates the transmitted, and arrows indicate the diffracted beams used for imaging. The upper right inset illustrates the wave vectors of the incident and diffracted beams, $\boldsymbol{k}_0$ and $\boldsymbol{k}$, the diffraction vector $\boldsymbol{K} = \boldsymbol{k} - \boldsymbol{k}_0$, and the corresponding reciprocal lattice vector $\boldsymbol{g}$.
(a) and (b) Images obtained with the (220) diffraction vector. In (b), the sample is tilted so that $\boldsymbol{K}$ differs from $\boldsymbol{g}$ by the excitation error $\boldsymbol{s} = \boldsymbol{K} - \boldsymbol{g}$. (c) and (d) Images obtained with the (2-20) diffraction vector. The imaged dislocation lines are always perpendicular to the diffraction vector chosen for imaging.

vectors. Instead of following this route, which would require large tilt angles that might destroy the crystal, we will use a simple argument here to determine the Burgers vector. We will verify this result by direct imaging of the dislocation topology by confocal microscopy in section 5.1.

In the fcc crystal structure, lattice translations are expected to occur along hexagonal close-packed planes, since these planes exhibit the highest in-plane density and therefore the shallowest potential wells. The observed dislocation lines along the [1-10] and [110] directions do indeed lie along these hexagonal close-packed planes. This is illustrated for the [1-10] line direction in figure 4.2a. To find a possible translation vector, we consider interparticle vectors along the hcp plane in figure 4.2b. The translation vector between adjacent wells of the hcp plane is 1/6 (112), and this is in fact the Burgers vector of the most frequently observed type of dislocation ("Shockley partial") in fcc metals. We therefore assume this vector to be the Burgers vector of the dislocations. The Burgers vector component parallel to the template is $b\cos\beta$, and the total misfit strain accommodated by the dislocations is $\varepsilon = b\Gamma\cos\beta$, where Γ is the number of dislocation lines per unit length. Using $b = 0.94\ \mu$m, $\cos\beta = 1/\sqrt{3}$, and $\Gamma^{-1} = 53\ \mu$m determined from figures 4.1a and c, we obtain $\varepsilon = 0.01$, which corresponds to two thirds of the misfit strain $\varepsilon_0 = 0.015$. To model the accommodation of misfit strain, we consider the strain energies in the crystal film. The total energy in the crystal film is given by the elastic energy due to the uniform strain of the film, and the energy associated with the incorporation of defects. In thin crystal films, the misfit strain is accommodated purely elastically, as shown by the absence of dislocations in films less than 22μm thick. The elastic energy increases linearly with the film thickness, so that at some critical thickness T_c, the crystal can lower its energy by incorporating dislocations that relieve some of the elastic strain. As the film thickness increases further, increasing portions of the misfit strain are accommodated by dislocations. To calculate the critical thickness, we consider the crystalline film to be an isotropic, linear elastic medium with Young modulus E, shear modulus μ, and Poisson ratio ν. The classical isotropic analysis by Frank and van der Merwe (1949) and Matthews and Blakeslee (1974) gives

$$T_c = \mu b \ln(R_0/r_0) \,/\, [4\pi E \varepsilon_0 (1-\nu)\cos\beta], \qquad (4.1)$$

where R_0 and r_0 are the outer and core radii of the dislocation strain field. We use $E/\mu = 2(1+\nu)$ for an isotropic elastic medium and take r_0 to be $b/4$ and R_0 to be the film thickness. Using $b = 0.94\mu$m, $\nu = 1/3$ (Frenkel and Ladd 1987) and $\varepsilon_0 = 0.015$, we obtain $T_c = 22\ \mu$m, in excellent agreement with the observation of dislocation formation in crystals thicker than 22 μm.

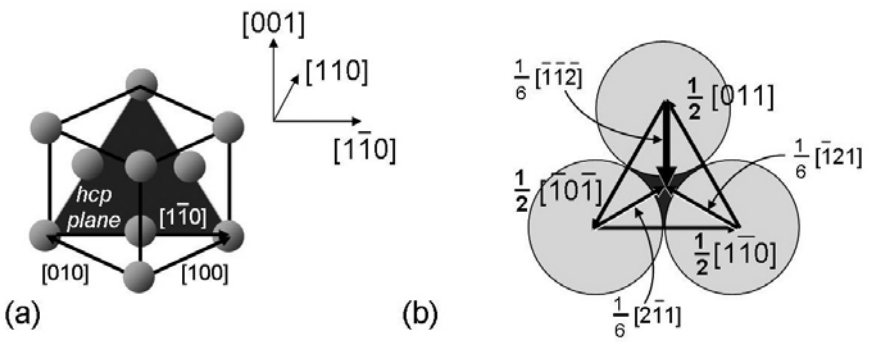

Figure 4.2 Fcc lattice: hexagonal close-packed plane and translation vectors
(a) Fcc unit cell and (-1-11) hexagonal close-packed plane parallel to the (1-10) direction. (b) Directions along the (-1-11) hexagonal close-packed plane shown in (a). The three arrows in the center of the triangle indicate vectors that connect adjacent wells in the hcp plane. The thick vertical arrow represents the vector -(1/6)(112), which is the Burgers vector of the dislocation with line direction along [1-10].

4.3 Imaging of dislocation propagation

4.3.1 Dislocation motion

The movement of a dislocation results in a permanent displacement of crystal parts above and below the plane of dislocation motion. The resulting permanent strain for a dislocation that moves a distance dx in a crystal with total cross section S is

$$\mathrm{d}\varepsilon = b dx / S, \tag{4.2}$$

where b is the magnitude of the dislocation Burgers vector. For ρ dislocations per unit area that move with average velocity v along parallel planes, strain is accommodated at a rate

$$(d\varepsilon / dt) = \rho b v. \tag{4.3}$$

The motion of these dislocations is driven by the glide force $\boldsymbol{F}_\mathrm{g}$ that results from the application of a shear stress. The force $d\boldsymbol{F}_\mathrm{g}$ exerted on a line element $d\boldsymbol{l}$ of the dislocation due to the applied shear stress τ is given by (Peach and Koehler 1950)

$$d\boldsymbol{F}_\mathrm{g} = - d\boldsymbol{l} \times (\tau \cdot \boldsymbol{b}). \tag{4.4}$$

This force is balanced by the friction force $\boldsymbol{F}_\mathrm{fr}$ associated with the motion of the dislocation through the lattice. In perfect crystals, the friction force is a periodic function of distance, thereby reflecting the periodicity of the lattice. The magnitude of the friction force depends on the nature of the interatomic bonding and on the dislocation core structure, and is not generally known. Peierls (1940) and Nabarro (1947) have suggested an analytical, nonlinear elastic model of a dislocation core that provides a simple estimate of the stress amplitude associated with a moving dislocation. It predicts that the dislocation energy per unit length oscillates with period $b/2$ and amplitude

$$E_\mathrm{p} = [\mu b^2 / \pi(1-\nu)] \exp(-2\pi w/b), \tag{4.5}$$

where w is the width of the dislocation core. E_p is known as "Peierls energy". The critical force per unit length required to move the dislocation through the periodic potential is given by the maximum slope of the periodic energy. This yields the critical glide stress

$$\tau_\mathrm{p} = 2\mu / [(1-\nu)\exp(-2\pi w/b)], \tag{4.6}$$

which is orders of magnitude smaller than the theoretical shear strength, $\tau = b\mu / (2\pi a)$ required for the translation of two rigid lattice planes in the absence of dislocations (Frenkel 1926). This model accounts for the observation that plastic yielding of many atomic crystals occurs at stresses much lower than their theoretical shear strength. The average dislocation velocity as a function of glide stress is, however, not easily determined. Since dislocation motion across the Peierls barrier is a thermally activated process that typically involves several material-dependant rate constants, the glide velocity as a function of glide stress cannot be determined in a general way. Velocitiy-stress relationships have been determined empirically by direct measurement of dislocation propagation for a wide range of stresses. These measurements show that for many materials, the dislocation velocity is a very sensitive function of the resolved shear stress and varies over many (~12) orders of magnitude. For many crystalline materials and wide ranges of stress, it is described by the empirical relation (Johnston and Gilman 1959)

$$v = C\tau^m, \tag{4.7}$$

where both C and m are material and temperature dependant (Haasen 1978). Equation (4.7) offers a simple empirical relation that describes the propagation of dislocations in atomic crystals. It provides a starting point for a constitutive description of the deformation of crystalline materials (Krauz and Krauz 1996).

For colloidal crystals, the friction force associated with dislocation motion can be estimated more easily. The main source of dissipation comes from the liquid matrix. Dislocation motion requires the motion of particles through the solvent, which induces hydrodynamic currents that give rise to a hydrodynamic friction force on the dislocation. This force should be fundamentally different for edge and screw dislocations: Since strong

damping occurs for all longitudinal modes in colloidal crystals (Hurd *et al.* 1982), edge dislocations are expected to be much less mobile than screw dislocations (Jorand *et al.* 1985). For screw dislocations, the friction force per unit length as a function of their velocity v_{screw} was estimated as (Jorand *et al.* 1985)

$$F_{fr} = [\,(\eta b^2) / (4\pi r_0^2)\,]\; v_{screw}\,, \qquad (4.8)$$

where r_0 is the dislocation core radius, and η the viscosity of the solvent.

This prediciton can be tested by using the LDM setup to follow the spreading of dislocations in strained colloidal films. Since the typical time constant for dislocation propagation is of the order of a few minutes, dislocations can be followed conveniently with the LDM setup by using a CCD camera that takes LDM images at video rate. Six snapshots from the LDM movie are shown in figure 4.3. These show the spreading of existing dislocations and the nucleation and growth of new ones. The growth of dislocations labelled by 1 through 4 is tracked exemplarily in figure 4.4a. A fast initial growth is followed by a slow, asymptotic approach to a final length L_f. This growth behavior reflects that initially, the elastic stress that drives the spreading of dislocations is large, but as dislocations grow to accommodate increasing amounts of the misfit strain, the local stress decreases so that dislocation growth eventually comes to a rest. The observed data is well described by

$$L = L_f\,(1 - \exp(-t/\xi)), \qquad (4.9)$$

where ξ is a characteristic time constant. This is shown by scaling each curve by its individual final length and time constant, and plotting $y = L / L_f$ as a function of $t' = t / \xi$ (figure 4.4b). The data collapse onto a single curve, well described by $y = 1 - \exp(-t')$ (solid line).

These measurements offer a unique opportunity to test the prediction of equation (4.8) for the friction force of a moving dislocation. The observed spreading of dislocations results from the lateral motion of screw segments that join the edge segment parallel to the template (figure 4.5). The uniform elastic strain ε_{el} of the film gives rise to the glide force (Matthews *et al.* 1970)

$$F_g = 2\mu(1+\nu) / (1-\nu)\, T\, b \cos\beta\, \varepsilon_{el}, \qquad (4.10)$$

which drives the motion of the screw segments along the hcp planes. The motion of the dislocation is resisted by the friction force F_{fr} according to (4.8), and by the dislocation line tension

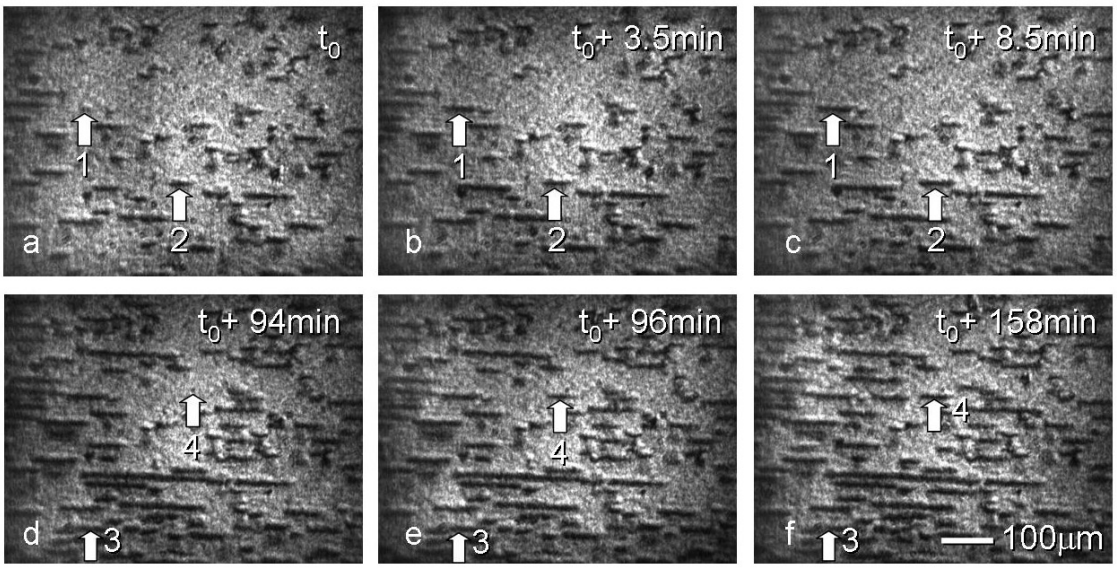

Figure 4.3 Dislocation propagation during epitaxial growth
Snapshots from an LDM movie show the spreading of dislocations during growth of a strained colloidal crystal film. Arrows mark four dislocations, whose growth is tracked and displayed in figure 4.4. The time t_0 corresponds to 14 hours after the final dose of particles was added to the crystal.

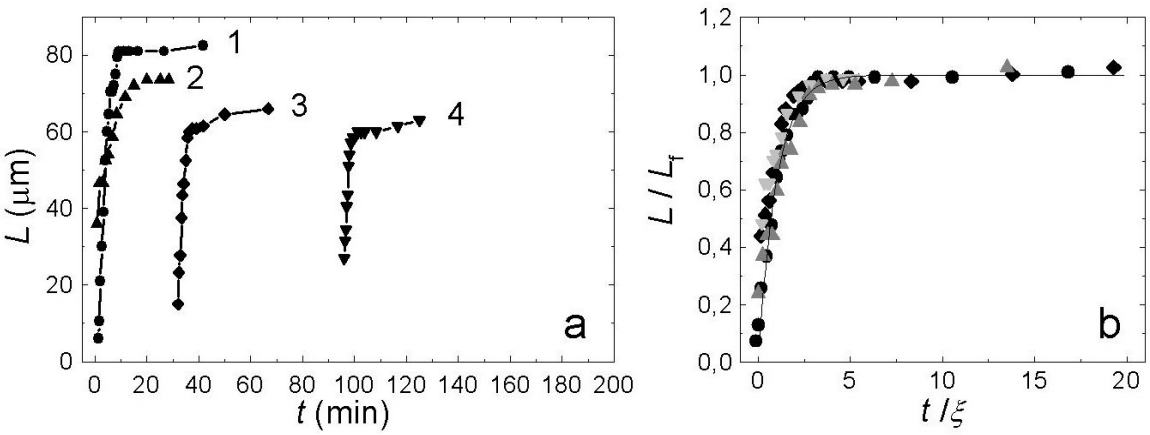

Figure 4.4 Dislocation growth
(a) Length as a function of time for the four dislocations marked in figure 4.3. (b) Rescaled dislocation length L/L_f versus rescaled time t/ξ for the four growth curves in (a). Individual constants $L_{f,i}$ and ξ_i are used to rescale each curve. The solid line has the functional form $[1-\exp(-t/\xi)]$.

$$F_l = [\mu b^2/(4\pi(1-\nu))]\ln(R_0/r_0). \tag{4.11}$$

As the dislocations move, they accommodate increasing portions of the misfit strain at a rate given by

$$\frac{d\varepsilon}{dt} = \rho_{\text{screw}}\, bv\cos\beta\,, \tag{4.12}$$

where ρ_{screw} is the number of mobile screw dislocations per unit area of the film. The length of a dislocation as a function of time can be calculated from the force balance $F_g = F_l + F_{fr}$. Using (4.10) to (4.12), and relation (4.8) for the friction force we find

$$\varepsilon(t) = \varepsilon_{\text{inf}}\,[1-\exp(-t/\xi)] \tag{4.13a}$$

where the constant

$$\varepsilon_{\text{inf}} = \varepsilon_0 - \{[(b\ln(R_0/r_0)/[8\pi(1+\nu)\,T\cos\beta)]\} \tag{4.13b}$$

corresponds to the final misfit strain accommodated by the dislocation, and the time constant

$$\xi = (1-\nu)\eta/4\pi r_0(E\cos^2\beta\sin\beta\,\rho_{\text{screw}}). \tag{4.13c}$$

This time dependence equals exactly the experimentally observed time dependence of the dislocation length, verifying the relation (4.8) for the friction force of a moving screw dislocation. We use the average value of ξ, which we determine to be 130 (±40) s to estimate the elastic modulus of the crystalline film. Using $\rho_{\text{screw}} = 3\cdot10^8\,\text{m}^{-2}$, determined from the number of spreading dislocations in the LDM images multiplied by two, and $\eta = 3\cdot10^{-3}$ Pa s we obtain a value of 0.3 Pa for the elastic modulus of the film. This value is in agreement with values obtained from molecular-dynamics simulations of hard-sphere crystals, which predict values of the order of 1 Pa (Frenkel and Ladd 1987).

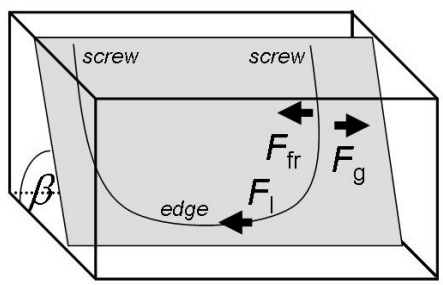

Figure 4.5 Forces that act on the dislocation line in the strained film
The schematic diagram shows a dislocation line along the hcp plane (grey) with edge and screw segments, and the forces that act on the dislocation line. β defines the angle between the hcp plane and the plane of the template.

4.3.2 Dislocation nucleation

In this section, we consider the application of inhomogeneous strain to study the formation of individual dislocations. An indenter is used to concentrate strain and localize dislocation formation in a small volume. As the indenter pushes into the crystal, it induces an inhomogeneous strain distribution of increasing magnitude, which ultimately causes nucleation of dislocations in the region of highest shear strain. Nanoindenters are used in experiments on atomic crystal films to concentrate strain in small crystal volumes that are initially defect-free. Direct imaging of dislocation formation during nanoindentation has been achieved by using a nanoindenter setup introduced in the beam path of the transmission electron microscope (Minor *et al.* 2002, Minor *et al.* 2006). These images provide an overview over the initial stages of defect formation and the development of dislocation structures. The experiments are, however, challenging because indentation has to be performed in remote inside the evacuated column of the electron microscope. Since the samples are very thin, typically 100-200 nm to be translucent for the electron beam they break easily, which makes these experiments very delicate.

Colloidal crystals allow indentation at larger length and time scales, and offer a more convenient way of imaging dislocations. A conventional sewing needle with a tip diameter of around 50μm serves as a "nanoindenter" for the colloidal crystal, and the LDM technique offers a convenient way to image the formation of dislocations on micrometer to millimeter length scales. Time series of LDM images taken during indentation of a colloidal crystal film allow direct observation of several stages of defect nucleation (figure 4.6). In this experiment, the needle is lowered at a very low speed of $10^{-5}\,\mu m\,s^{-1}$ to allow enough time for thermally activated defect nucleation. When the needle touches the crystal, two dark regions beneath the tip appear, which indicate the induced elastic strain (figure 4.6b). Remarkably, these regions exhibit intensity fluctuations that last several minutes, giving direct evidence of strain fluctuations associated with the thermal motion of the particles. The nucleation of a dislocation loop is indicated by a dark spot about 8 μm in radius that appears below the needle tip after 230 min (figure 4.6 c). This loop grows in size and detaches from the needle (figure 4.6d). The LDM images further show the formation of many more loops, and the evolution of a complex dislocation structure at later stages of indentation (figures 4.6e and f).

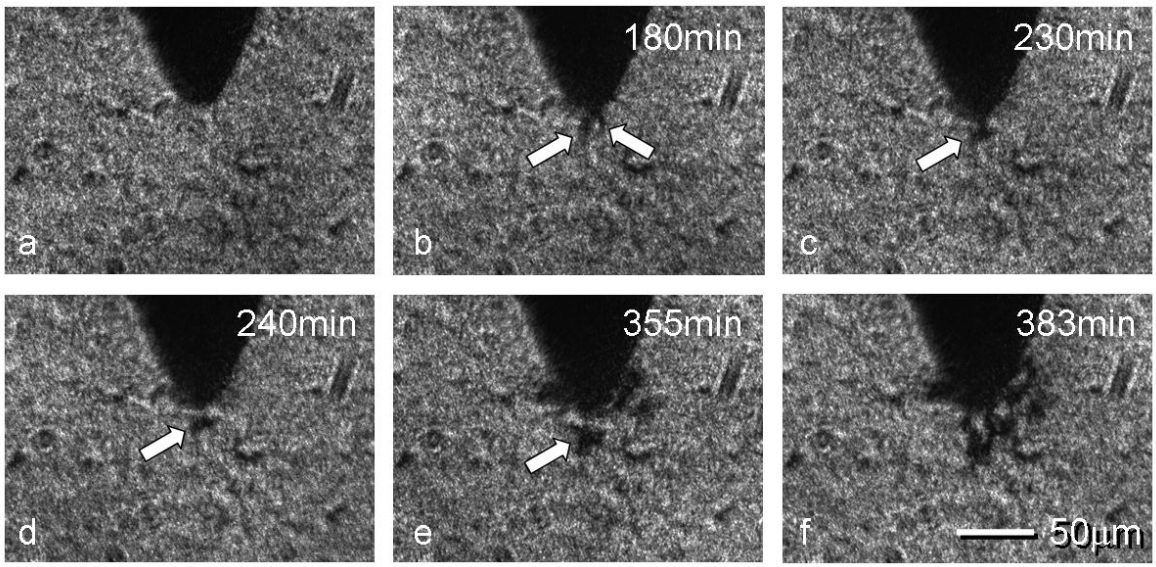

Figure 4.6 Dislocation propagation during indentation
Snapshots from a laser diffraction microscope movie show the nucleation of a dislocation loop (b)-(d), and the evolution of the dislocation structure (e,f) during indentation of a colloidal crystal film.

5. Confocal microscopy of defects

While LDM allows for convenient imaging of dislocations on intermediate length scales, it does not provide insight into the nature of the defects at the particle scale. Such information is, however, needed for the development of models that aim at describing dislocation propagation quantitatively. For atomic systems, insight into the topology of dislocations at the atomic scale is obtained with high-resolution transmission electron microscopy (HRTEM). This technique has lead to important insight into dislocation core structures in various crystalline materials (Mills *et al.* 1994 and references therein). HRTEM images atomic columns along high symmetry directions of the crystal. This technique provides a projection of core structures of dislocations that are oriented with line directions parallel to the beam direction.

For colloidal systems, three-dimensional imaging of the crystal lattice is possible with confocal microscopy. This technique allows visualization of the individual colloidal particles and crystal defects in three dimensions. In dense suspensions, where particle diffusion is slow, fast confocal microscopy allows for following the individual colloidal particles, and determining their three-dimensional trajectories. Combined with confocal microscopy, colloidal systems provide powerful *analogue computers*, which due to their vast parallel processing efficiency allow modeling of phenomena of a size and scale that are difficult to achieve by digital computation.

We will focus on the application of confocal microscopy to elucidate dislocation structures and dynamics. The particle positions determined with confocal microscopy allow reconstruction of the defect topology and the three-dimensional strain distribution that drives the nucleation of defects. Fast confocal microscopy offers a detailed view at dislocation dynamics: individual, thermally driven dislocation nucleation events can be observed in three dimensions and real time. Simultaneous imaging of the strain distribution offers insight into the interplay between local strain and thermal fluctuations that governs the nucleation of defects.

5.1 Dislocation topology

Confocal microscopy provides unique images of the colloidal crystal lattice at the particle scale. Stacks of confocal images acquired at increasing depth into the sample reveal the positions of the individual particles in three dimensions, and particle tracking software is used to determine the positions of the particle centers with an accuracy of 20 nm in the horizontal, and 50 nm in the vertical direction (Crocker and Grier 1996, Dinsmore *et al.* 2001). Crystal defects are identified from the nearest neighbour configuration of the particles. Stacking faults along the hexagonal close-packed planes, where the stacking order changes from the fcc stacking ABCABC to the hcp stacking ABAB, manifest in the number of opposing nearest neighbor pairs: Particles at the stacking fault have three opposing nearest neighbors as is the case in the hcp lattice rather than six as in the fcc lattice (Kelchner *et al.* 1998, Schall *et al.* 2004). A plot of all particles with three opposing nearest neighbors reveals the stacking fault structure in strained fcc colloidal crystals. This is shown for a 60 μm by 60 μm by 30 μm reconstruction of the uniformly strained film in figure 5.1a. The particles align along hexagonal close packed planes, thereby delineating stacking faults along these planes. A typical *y-z* section through a stacking fault is shown in figure 5.1b. This crystal section shows that the stacking fault ends above the template and is terminated by a dislocation. The first row of particles sits in the template holes. Already in the second row of particles, we observe the emergence of a strain field associated with a dislocation line perpendicular to the *y-z* plane. The dislocation core (⊥) lies about two particle diameters

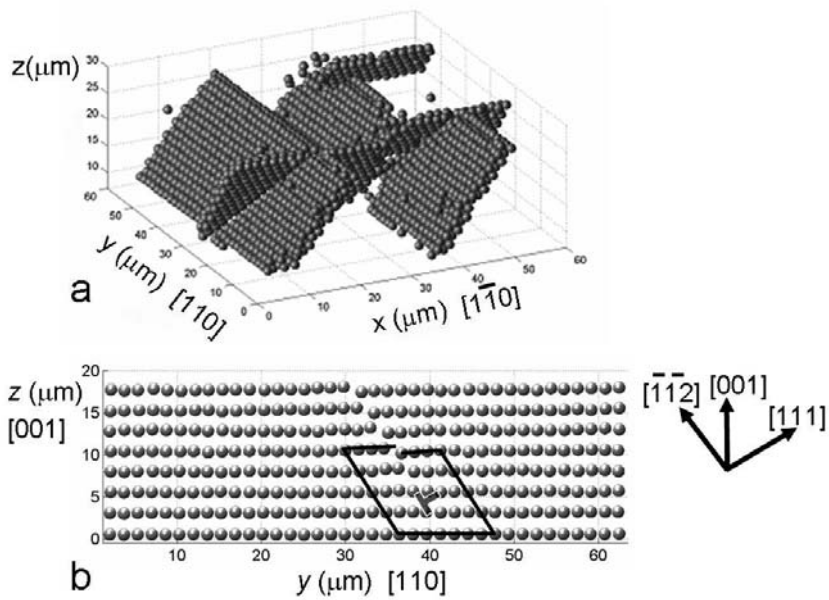

Figure 5.1 Defect structure in the strained colloidal crystal film
(a) Reconstruction of defects in a 55 μm by 55 μm by 25 μm crystal section. The particles show stacking faults along hcp planes of the fcc crystal film. (b) Reconstructed *y*-*z* section through a stacking fault. The stacking fault is terminated by a dislocation, whose core is indicated by ⊥. The black loop illustrates the Burger circuit.

above the template. The dislocation is characterized by a Burgers circuit (black line), which closes in the perfect lattice, but exhibits a closure failure around the dislocation core. The dislocation Burgers vector is obtained by connecting the starting and ending points of the Burgers circuit. Evaluation of the Burgers circuit in figure 5.1b yields $\boldsymbol{b} = 1/6(-1-12)$, which is indeed equivalent to the vector 1/6(112) anticipated in section 4.2. This type of dislocation is known as a Shockley partial dislocation, and is the most prominent type of dislocation in fcc metals (Hirth and Lothe 1982). In contrast to fcc metals, where Shockley partial dislocations typically appear in pairs to limit the extent of the stacking fault, in colloidal crystals the stacking faults are not limited by another dislocation, and extend to the crystal surface. This reflects the vanishingly low energy cost of stacking faults in hard-sphere crystals (Pronk and Frenkel 1999).

The offset of the dislocation from the template can be quantitatively adressed by considering the forces that act on the dislocation line. Because the first row of particles is fixed by the template, this gives rise to an image force that repels the dislocation from the rigid boundary. This force is given by (Hirth and Lothe 1982)

$$F_{\mathrm{i}} = \mu b'^2 / [4\pi(1-\nu)z], \qquad (5.1)$$

for a dislocation at height z, whose Burgers vector b' is parallel to the template. On the other hand, the elastic strain of the crystal layers below the dislocation, which are still strained, results in the elastic force

$$F_{\mathrm{el}} = (1/2)\, E\varepsilon_0^2 / \Gamma \qquad (5.2)$$

that drives the dislocation towards the template. The forces balance at the height

$$z_0 = \mu (b\cos\beta)^2 \Gamma / [2\pi E(1-\nu)\varepsilon_0^2], \qquad (5.3)$$

where the dislocation comes to rest. We neglect the Burgers vector component perpendicular to the template, and use $E/\mu = 2(1+\nu)$ with $\nu = 1/3$, and $E = 0.3$ Pa and $\Gamma^{-1} = 53$ μm determined with LDM (sections 4.2 and 4.3). We obtain $z_0 = 2.1$ μm, in very good agreement with the height estimated from figure 5.1b, indicating that the continuum description holds even for a very small number of layers.

5.2 Strain distribution

Continuum models are widely used to describe the propagation of dislocations in atomic crystals on medium-range length scales (Hirth and Lothe 1982). A general continuum description of dislocation propagation involves the local strain, which provides the driving force for dislocation propagation. While at the atomic scale, the interatomic potential determines the dislocation structure, on a medium-range length scale, the strain field determines the propagation and interactions of dislocations, which ultimately determines the deformation of the crystal on a macroscopic scale. Continuum models are used to describe the interactions of dislocations mediated by their strain fields.

Since colloidal crystals exhibit a finite stiffness, the application of any small strain to the crystal results in a finite stress, which according to equation (4.4) provides the driving force for dislocation propagation. Therefore, in analogy to ordinary crystalline materials, the continuum description may provide a useful tool to describe defect propagation in these soft materials (Schall *et al.* 2004, 2006). We have seen in the last paragraph that continuum theory applies to describe dislocations even on length scales of a few particle diameters. Here, we will embark on the continuum description, and use the three-dimensional particle positions determined with confocal microscopy to determine the local strain field. This calculation provides a unique visualization of strain fields in deformed crystals, thereby allowing insight into the interplay of strain distribution and defect propagation.

To determine the strain distribution, the local strain tensor of each particle is calculated from the local configuration of the particle. For each particle, we determine the vectors $\boldsymbol{d}_i$ to its nearest neighbours and compare them with those of the ideal fcc lattice $\boldsymbol{D}_i$. The best affine deformation tensor α that transforms the ideal vectors $\boldsymbol{D}_i$ to the real vectors $\boldsymbol{d}_i$ is then determined by minimizing the mean square difference $\sum_i (\boldsymbol{d}_i - \boldsymbol{\alpha D}_i)$ (Falk and Langer, 1998). The symmetric part of α corresponds to the local strain of the particle under consideration. To smooth the resulting strain distribution, the strain tensor for each particle is averaged with those of its nearest neighbors, and the resultant average strain tensor, ε_{ij}, is assigned to the particle under consideration.

The final strain values show a uniform distribution for defect-free crystal films, but exhibit a strongly non-uniform distribution after defects have formed. Each defect introduces a characteristic strain distribution. We focus on the defects in the uniformly strained film to visualize the strain distribution of long, straight edge dislocations. The distribution of the

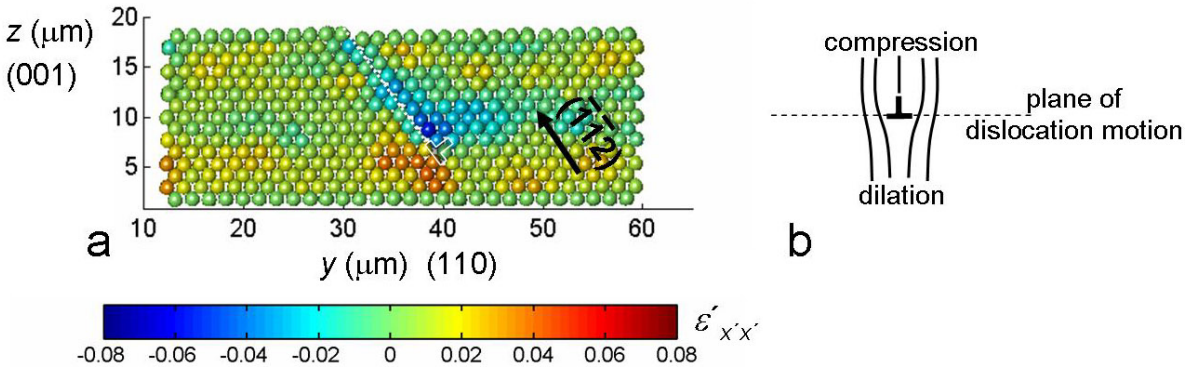

Figure 5.2 Strain distribution of a long, straight edge dislocation
(a) *y*-z section shows the distribution of the normal strain $\varepsilon'_{x'x'}$ along the (-1-12) direction around a long, straight edge dislocation in the strained crystal film (see color scale). The dashed line indicates the stacking fault plane bounded by the dislocation. (b) Schematic diagram shows zones of compression and dilation associated with a long, straight edge dislocation.

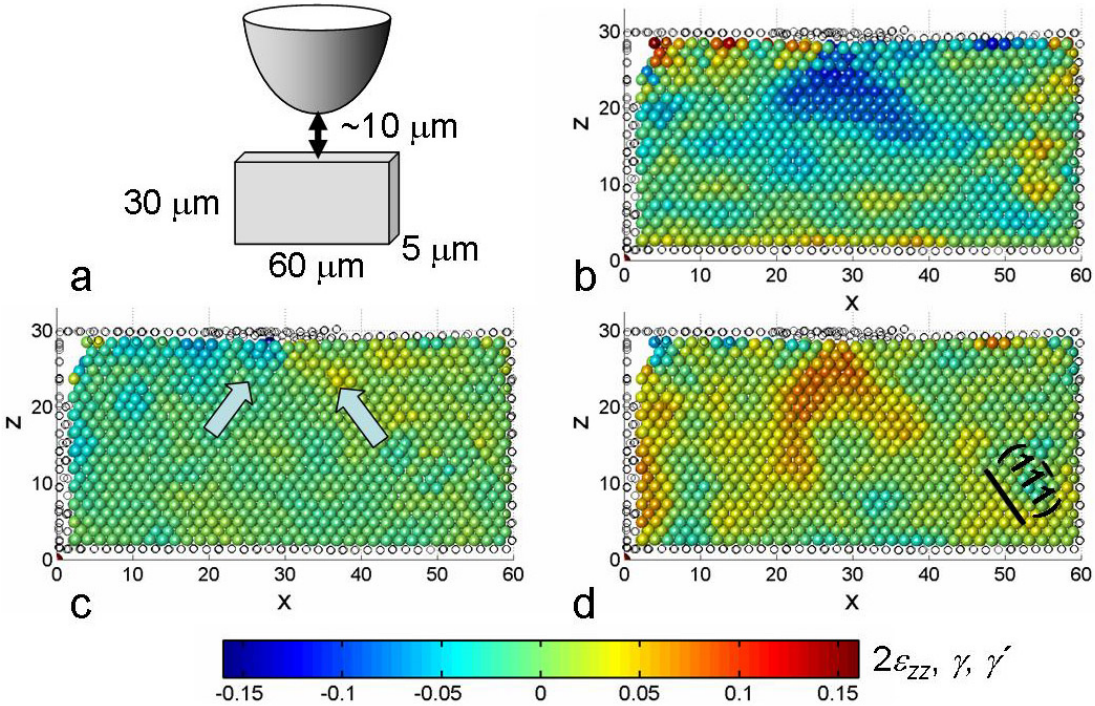

Figure 5.3 Strain distribution in the indented crystal film
(a) Schematic showing the position of the needle with respect to the reconstructed 60 μm by 5 μm by 30 μm crystal sections shown in (b) – (d). (b) – (d) 5 μm thick sections centered below the needle show the distribution of the compressive strain ε_{zz} (b), the shear strain $\gamma = 2\varepsilon_{xz}$(c), and the shear strain component $\gamma' = 2\varepsilon'_{x'z'}$ on the (1-11) plane along the [1-1-2] direction (d).

normal strain ε_n along the [-1,-1,2] Burgers vector direction is determined by calculating the strain tensor ε_{ij}' in a rotated coordinate system, in which the x' and z' axes align with the (-1-12) and (111) directions, respectively, and by taking $\varepsilon_n = \varepsilon'_{x'x'}$. Particle colors illustrate the distribution of ε_n in figure 5.2a. This distribution shows zones of local dilation (red spheres) and compression (blue spheres) on opposite sides of the stacking fault plane, as expected for a long straight edge dislocation (figure 5.2b). While for a dislocation in the bulk, the zones of dilation and compression are expected to be symmetric with respect to the slip plane (Hirth and Lothe 1982), the red and blue zones do not appear to be symmetric with respect to the stacking fault plane. This asymmetry is caused by the proximity of the rigid boundary, which modifies the strain distribution.

It is particularly insightful to visualize the strain distribution of the indented film. We focus on a crystal section below the indenter (figure 5.3a) to visualize the induced elastic strain in the early deformation stage before the first defect forms. This stage corresponds to the LDM image shown in figure 4.6b. 60 μm by 5 μm by 30 μm reconstructions of the strain distribution show that the needle introduces strongly non-uniform strain with pronounced compressive and shear strain components (figure 5.3b to d). Blue spheres that concentrate in a region below the needle indicate a zone of compressive strain in figure 5.3b. Light blue and yellow spheres indicate zones of negative and positive shear strain to the left and right of the indenter in figure 5.3c. The positions of the shear strain maxima are in agreement with Hertzian theory, which describes the deformation of an elastic material under a spherical indenter (Hertz, 1881). Dislocation nucleation is driven by the shear strain component along the hcp plane. To illustrate the corresponding strain distribution, as an example, the distribution of the shear strain component γ' along the (1-11) plane is shown in figure 5.3d.

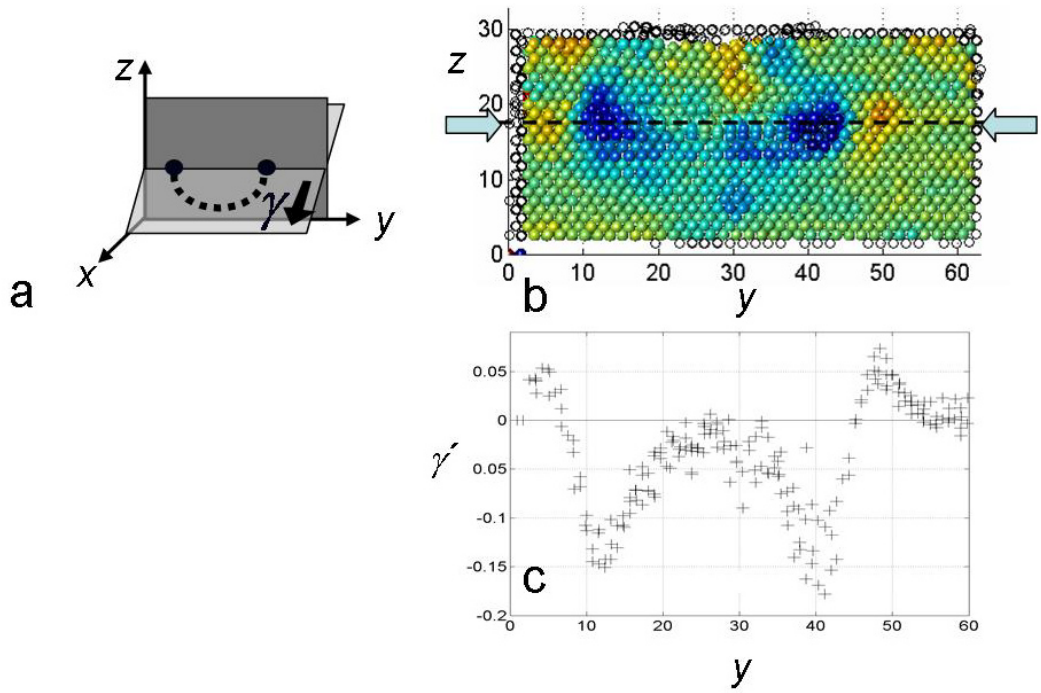

Figure 5.4 Strain distribution in the indented crystal film after the nucleation of a dislocation loop
(a) Schematic showing the dislocation loop (dotted line) with respect to the *y*-*z* crystal section (dark grey) shown in (b). The y-z plane shown in (b) intersects the dislocation loop along its diameter. (b) Distribution of the shear strain γ' along the (1-11) plane in a 5 μm thick *y* - *z* crystal section that intersects the dislocation loop along its diameter.(c) Shear strain values versus *y* for particles within 1.6 μm of the dashed line in (b).

This shear strain component drives the nucleation of Shockley partial dislocations along the (1-11) plane. The distribution of γ' shows a region of high positive shear strain (red) centered approximately 10 μm below the needle with an average value of γ' of roughly 0.06. Remarkably, the shape of this strain distribution matches the contrast profile observed with LDM (figure 4.6b).

Drastic changes occur in the strain distribution as defects nucleate. These changes have important consequences for subsequent dislocation nucleation as they guide the formation of defects. The evolution of the dislocation arrangement results from the subtle interplay of the applied strain imposed by the needle and the strain fields of the individual defects. The colloidal model allows us to track the changes in the strain distribution and elucidate the role of strain modifications in guiding subsequent dislocation nucleation. We illustrate this interplay by showing the distribution of γ' after the nucleation of the first dislocation in figure 5.4. The γ' distribution is shown for a crystal plane that intersects the nucleated dislocation loop along its diameter (figure 5.4a and b). Formation of the loop results in negative shear strain inside the loop (dark blue spheres), and positive shear strain outside (orange spheres adjacent to the blue zones). A plot of the strain values as a function of *y* for all particles within 1.6 μm from the dashed line (figure 5.4c) reveals a characteristic strain distribution of a dislocation loop (Marcinkowski and Sree Harsha 1968). The strain diverges on both sides of the dislocation with the divergence truncated at the dislocation core. The crossover at $y = 5$ μm and $y = 45$ μm, where γ' switches sign, demarcates precisely the intersection of the dislocation line with the *y*-*z* plane. Comparison of figs. 5.4b and 5.3d shows that the negative shear strain induced by the loop reduces the cumulative strain due to the indenter, thereby decreasing the driving force for dislocation nucleation on the same hcp plane. This causes nucleation of the second dislocation to occur on the adjacent, intersecting hcp plane, as shown by imaging the defect configuration during indentation with confocal microscopy (section 5.3).

5.3 Thermally activated defect nucleation

The inhomogeneous strain distribution induced by an indenter (figure 5.3) localizes defect nucleation in small volumes, allowing investigation of defect nucleation in the bulk of perfect crystals. Nanoindentation on atomic crystals take advantage of this strain disribution to investigate incipient plasticity, i.e. dislocation nucleation in volumes that are initially defect-free. Force-displacement measurements are used to detect the formation of dislocations. Careful measurement of the tip displacement as a function of applied load offers sufficient resolution to identify individual displacement steps associated with the nucleation of single dislocations (Gouldstone *et al.* 2000, Suresh *et al.* 1999). Nanoindentation offers the advantage that simulation length scales reach almost experimental length scales allowing unique comparison of simulation results and experimental observation (Gannepalli and Mallapragada 2002, Kelchner *et al.* 1998a,b, Lilleodden *et al.* 2003, Schuh 2006). As an important result of this direct comparison, the initial stages of defect formation were associated with the homogeneous nucleation of dislocation loops in the bulk of the crystal at stresses close to the ideal shear strength of the material (Li *et al.* 2002).

The forces applied in analogue indentation experiments on colloidal crystals are very small, of the order of piconewtons, and cannot be measured. Dislocation nucleation can, however, be directly visualized with confocal microscopy. This technique allows resolution of individual, thermally driven defect fluctuation events. To observe these, defects are identified from their distorted nearest neighbor configuration as described previously. Three-dimensional reconstructions of the defect configurations are shown in figure 5.5b to e. The first defect nucleus appears after 98 min (figure 5.5b). This defect is not stable and disappears after a few minutes. After the appearence and disappearence of five such nuclei, a stable defect finally nucleates (figure 5.5c) and grows (figure 5.5d). The final defect structure after 154 min shows a second defect, which nucleated on an intersecting hcp plane (figure 5.5e).

Traces of the dislocation lines that surround the stacking faults are determined precisely from the three-dimensional confocal microscope images. These are shown in figure 5.5f. The traces show that the radius of the unstable defect (figure 5.5f, light gray dots) is approximately 5 μm, while that of the stable defect (figure 5.5f, dark gray dots, small loop) is 7μm. Therefore, defects with a radius larger than roughly 6 μm are stable and grow.

The observed defect nucleation reflects a competition between the energy cost for creating a dislocation loop and the energy gain from the strain relieved by the formation of the loop. The energy cost associated with the formation of a dislocation loop with radius r is $B(\mu b^2 r/2)\ln(r/r_0)$, where r_0 is the effective core radius of the dislocation strain field, and $B = 5/4$ is a constant that accounts for the mixed edge-screw topology of a dislocation loop (Hirth 1963). The energy gain from relief of the overall strain is $\pi r^2 b\tau$, where πr^2 is the area inside the loop. The total energy reaches a maximum at the critical loop radius

$$r_c = (Bb/4\pi\gamma')\ln(r_c/r_0), \qquad (5.4)$$

with the critical energy at $r = r_c$

$$U_c = B(\mu b^2 r_c/4)\ln(r_c/r_0). \qquad (5.5)$$

Here, we have used $\gamma' = \tau/\mu$. Dislocation loops with $r<r_c$ are not stable and reduce their total energy by shrinking, while dislocation loops with $r>r_c$ are stable and reduce their total energy by growing. We substitute $r_0 = b\exp(-1.4)$ for the effective core radius (Hirth 1963), and use $\gamma' = 0.06 \pm 0.01$ in the high shear region (figure 5.3d). This yields $r_c = (5.0 \pm 1.5)\,b$ and $U_c = (1.6 \pm 1.0)\,\mu b^3$. These values can be compared with the observed critical defect size and nucleation rate. Using $b = 0.94$ μm, the model predicts $r_c = (4.7 \pm 1.4)$ μm, in good agreement

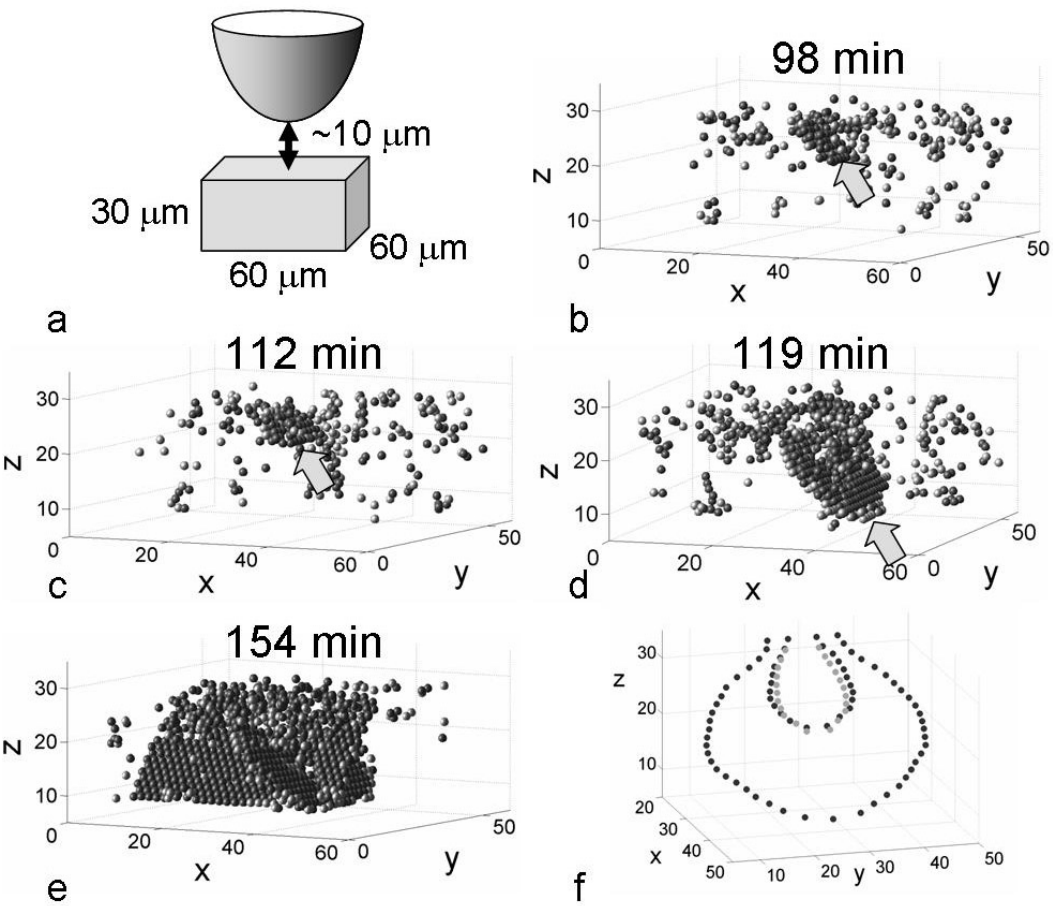

Figure 5.5 Defect nucleation at the particle scale
(a) Schematic showing the position of the needle tip with respect to the 60 μm by 60 μm by 30 μm crystal section depicted in (b) to (e). (b)-(e) 60 μm by 60 μm by 30 μm reconstructions show defect formation at the particle scale. The spheres depict particles with distorted nearest neighbor configurations. Arrows indicate stacking faults that are bound by Shockley partial dislocations. (f) Traces of the dislocation lines that surround the defects in (b) to (d). Light grey dots: trace of defect shown in (b); dark grey dots: traces of defects in (c) and (d).

with the observations of $r_c \approx 6\mu m$. The value of the nucleation energy can be compared with the observed nucleation rate J using

$$J = \nu_0 m \exp(-U_c/kT). \qquad (5.6)$$

where m is the total number of particles in the high-stress region. The nucleation rate is estimated from the average time $t_{fluct} \approx 8$ min between fluctuations to be $J = 2 \times 10^{-3} s^{-1}$. The attempt frequency ν_0 is determined from the average time between particle collisions, which equals the time t_{diff} required for a particle to diffuse in its local well until it reaches its nearest neighbor. Using $t_{diff} = (\pi\eta a\Delta^2 / kT)$, where the distance between nearest neighbours $\Delta \approx 0.08$ μm is estimated from the crystal lattice constant and the particle diameter, and the solvent viscosity $\eta = 3 \cdot 10^{-3}$ Pas, we obtain $t_{diff} \approx 10^{-2}$s or $\nu_0 = 100\ s^{-1}$. The number of particls in the high shear region is determined from the observation that the high shear region extends about five particle diameters in the x, y and z-directions. Hence, $m = 125$. Using these values and equation (5.6), we obtain $U_c = 16\,kT$. The value predicted by the model is $U_c = (35 \pm 20)\,kT$, where we have used $\mu = E/[2(1+\nu)]$ with $\nu = 1/3$ and the measured value $E = 0.3$ Pa. Thus, the value predicted by the model is a factor of two higher than that determined from the measured nucleation rate, but still in reasonable agreemeent with the measurement.

6 Simulation of diffraction image contrast of dislocations

In this chapter, we provide a link between LDM and confocal microscopy and use the three-dimensional particle positions determined with confocal microscopy to simulate LDM image contrast. The contrast produced by defects encodes the particle displacement field associated with these defects. By using image simulation techniques we are able to establish a link between this displacement field and LDM contrast features.

Diffraction contrast calculations of atomic crystal defects have been intrumental to understand TEM image contrast. They have layed the ground for proper interpretation of TEM images to determine the defect type, and its location and orientation (Whelan and Hirsch, 1957a,b, Hirsch *et al.* 1960, Howie and Whelan, 1962), as well as properties of the crystal such as its thickness and local bending (Heidenreich 1949). Calculations of diffraction contrast of dislocations are based on continuum models of these defects, allowing simulation of image contrast as a function of important parameters such as the Burgers vector and line direction of the dislocation, and imaging conditions.

Colloidal crystals offer the advantage that the individual particles can be imaged in three dimensions with confocal microscopy so that the three-dimensional displacement field of defects is directly accessible. Hence, no model for the dislocation strain field is needed and LDM images can be calculated from the actual positions of the particles, enabling direct comparison of experimental and calculated image contrast. In this chapter, we apply simple kinematical theory of diffraction contrast to reproduce basic features of LDM images. The use of kinematical theory is justified by the close refractive index match of the particles and the suspending solvent and the small thickness of the crystal, which both limit the amount of multiple scattering.

Image simulation techniques used for the calculation of TEM diffraction image contrast will be briefly discussed in section 6.1, while details of the LDM image simulations will be described in 6.2.

6.1 Image simulation techniques

Several image simulation techniques have been used to exploite the relation between defect strain field and image contrast, and a description of these techniques is beyond the scope of this review. There are excellent textbooks that describe diffraction contrast image formation (Hirsch *et al.*, 1965) and the practical use of TEM to analyze crystal defects (Williams and Carter 1996). Dynamical diffraction theory has been applied to reproduce many hallmark features of diffraction contrast images. This theory, formulated in a form suitable for numerical computation (Howie and Whelan, 1961), has been applied to describe the contrast of stacking faults (Whelan and Hirsch, 1957a,b), of long, straight dislocations (Howie and Whelan, 1962), and dislocation loops (Bullough *et al.*, 1971, Maher *et al.*, 1971, Eyre *et al.*, 1977, Saldin *et al.*, 1979a,b). Beam intensities are computed at a grid of points on the electron exit surface of the crystal foil using the column approximation, which determines the image intensity at points P' from the scattering of all atoms in a narrow column centered at P' (Hirsch *et al.* 1960). These calculations, which are based on continuum models of dislocation strain fields, have enabled proper interpretation of transmission electron microscope images, thereby making conventional transmission electron microscopy a powerful tool to investigate defects and defect mechanisms in crystalline materials (Williams and Carter 1996).

Of recent interest has been the calculation of diffraction contrast of small centers of strain, such as small dislocation loops and stacking fault tetrahedra. Such defects are formed

when a material is irradiated with energetic particles. The creation of these defects and their properties have been intensively studied by TEM because of their technological relvance for the mechanical properties of materials in nuclear reactors. The small size of these defects, however, prohibits the use of continuum models and conventional diffraction contrast calculations. Molecular dynamics simulations have been used to generate small defect clusters, and diffraction image contrast has been calculated directly from the simulated defect configurations (Schäublin *et al.* 2000). Because these defects have sizes of the order of a few lattice constants only, the column approximation is no longer suitable for image simulation, and the authors use an alternative image simulation method, the "multislice method" (Cowley and Moodie, 1957). The resulting images show good agreement with experimental diffraction image contrast obtained with TEM.

Within this review, we will use the most basic technique to compute laser diffraction image contrast: Kinematical diffraction theory and the column approximation will be applied to calculate diffraction image contrast from the three-dimensional positions of the colloidal particles determined with confocal microscopy.

6.2 LDM image simulations

The long, straight dislocations that form in uniformly strained films are well suited for the investigation of image contrast. We focus on an isolated defect, and determine particle positions in a 60 μm by 60 μm by 18 μm crystal section centered around this defect. Three-dimensional reconstructions of the isolated defect and the defect embedded in the crystal are shown in figures. 6.1a and b. Dark grey particles demarcate particles that sandwich a stacking fault along the hexagonal close-packed plane.

We consider a laser beam with wavelength $\lambda = 632.8$ nm that scatters from the crystal film. The amplitude of a diffracted beam at a point P below the crystal is determined from the positions $\boldsymbol{r}_{\mathbf{m}}$ of all particles within a narrow column centered at P according to (3.34). We chose a column of radius 3.0 μm, which contains a sufficient number of particles. Substitution of $\boldsymbol{K}$ and $\boldsymbol{s}$ according to (3.27) and (3.31) yields the dependence of the image amplitude on the excitation error $\boldsymbol{s}$. For a perfect crystal, the intensity $I \propto |A|^2$ as a function of excitation error should oscillate as $\sin^2(\pi T s)/(\pi s)^2$ (see chapter 3.3.1). This relation can be tested by determining the intensity as a function of s for a column in a defect-free crystal region. We choose a column centered at $P_0 = (18,28)$ (arrow and shaded area in figure 6.1b), and show a reconstruction of the isolated particle column for $s = 0$ in figure 6.1 c. The resulting intensity as a function of s is shown in figure 6.1d. This curve does indeed closely follow a relation of the form $I(s) \sim \sin^2(\pi T s)/(\pi s)^2$ as expected for the relation between the diffracted beam intensity and the excitation error. $I(s)$ has minima at $Ts_m = m$, where m is an integer number. Therefore, the location s_1 of the first minimum indicates the inverse crystal thickness. From $s_1 = 0.057\ \mu\text{m}^{-1}$, we determine $T = 17.5$ μm in good agreement with the actual height of the crystal section of 18 μm (figure 6.1b).

Let us now turn to the calculation of LDM image contrast. This is achieved by calculating the intensity distribution $I(x,y) = A^2(x,y)$ at a grid of points $P = (x,y)$ across the crystal section. The wave vectors $\boldsymbol{k_0}$ and $\boldsymbol{k}$ are chosen to match closely the directions of the incident and diffracted beams of the experiments. The incident beam with wave vector $\boldsymbol{k_0}$ is chosen under an angle of 22.8° to the z-axis, resulting in a symmetric configuration of the incident and diffracted beam, where the diffracted beam leaves the crystal under the same angle (figure 6.2a). Images are calculated for the diffraction vectors $\boldsymbol{g}_1$=(220) and $\boldsymbol{g}_2$=(2-20) and excitation errors $s = 0$ and $s = 0.07\ \mu\text{m}^{-1}$. These are compared with experimental LDM images in figure 6.2.

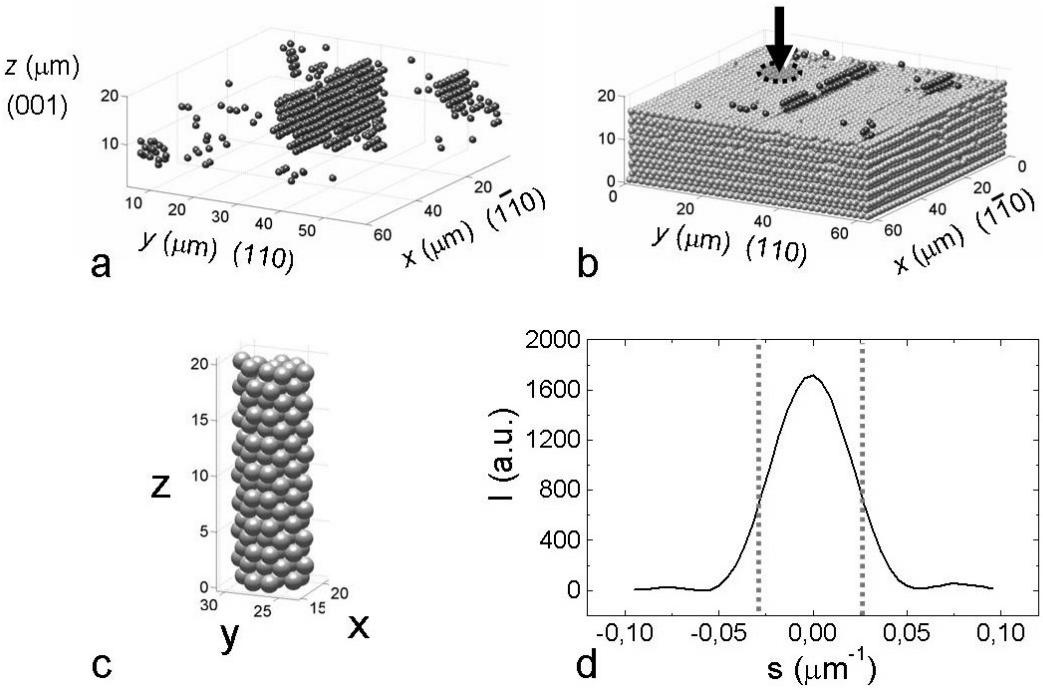

Figure 6.1 Simulation of diffraction contrast of a crystal defect
(a) and (b) Reconstructions of a 60 μm by 60 μm by 17 μm crystal section showing the defect configuration at the particle scale. Dark grey particles demarcate stacking faults. (a) Isolated stacking faults (b) Stacking faults embedded in the otherwise perfect fcc crystal. Arrow and shaded area indicate crystal column in a defect-free crystal region. (c) Isolated crystal column for $s = 0$ used to calculate the diffracted beam intensity as a function of excitation error depicted in (d). (d) Diffracted beam intensity as a function of excitation error s.

Dark lines on a bright background demarcate the defects in figure 6.2b, obtained for $\boldsymbol{g}_1$=(220) and $s = 0$. The simulated image contrast resembles the experimental contrast observed with LDM at maximum diffracted beam intensity (figure 6.2d). The diffraction vector $\boldsymbol{g}_2$=(2-20) perpendicular to $\boldsymbol{g}_1$ is used to explore the visibility of the defect. Since $\boldsymbol{g}_2$ lies along the x-axis and the dislocation Burgers vector is perpendicular to the x-direction, both are perpendicular to each other. The resulting simulated image shows no contrast (figure 6.2c), thereby verifying the invisibility condition $\boldsymbol{g} \cdot \boldsymbol{b} = 0$ for dislocations. The absence of any residual contrast in figure 6.2c demonstrates that the particle displacements associated with the defect are strictly perpendicular to the dislocation line, in agreement with the experimental observations.

The images simulated for the excitation error $s = 0.07\ \mu\text{m}^{-1}$ show inversion of the image contrast (figure 6.2e and f) as observed in the experiments, where the crystal is tilted slightly to decrease the diffracted beam intensity. The value of s chosen here is close to the first minimum of the $I(s)$ curve (figure 6.1 d), and results in maximum image contrast. The resulting image for $\boldsymbol{g}_1$=(220) shows good agreement with the corresponding LDM image of the crystal tilted slightly to produce a strong inverted contrast (figure 6.2 g). No defect contrast is observed for the diffraction vector $\boldsymbol{g}_2$ perpendicular to the dislocation Burgers vector (figure 6.2 f), confirming again the invisibility of the dislocation under the condition $\boldsymbol{g} \cdot \boldsymbol{b} = 0$.

A more rigorous test of simulated image contrast is achieved by comparing the width of the dislocation contrast with that in the experimental images. Such a comparison has been used to test the applicability of kinematical theory to describe TEM image contrast. This

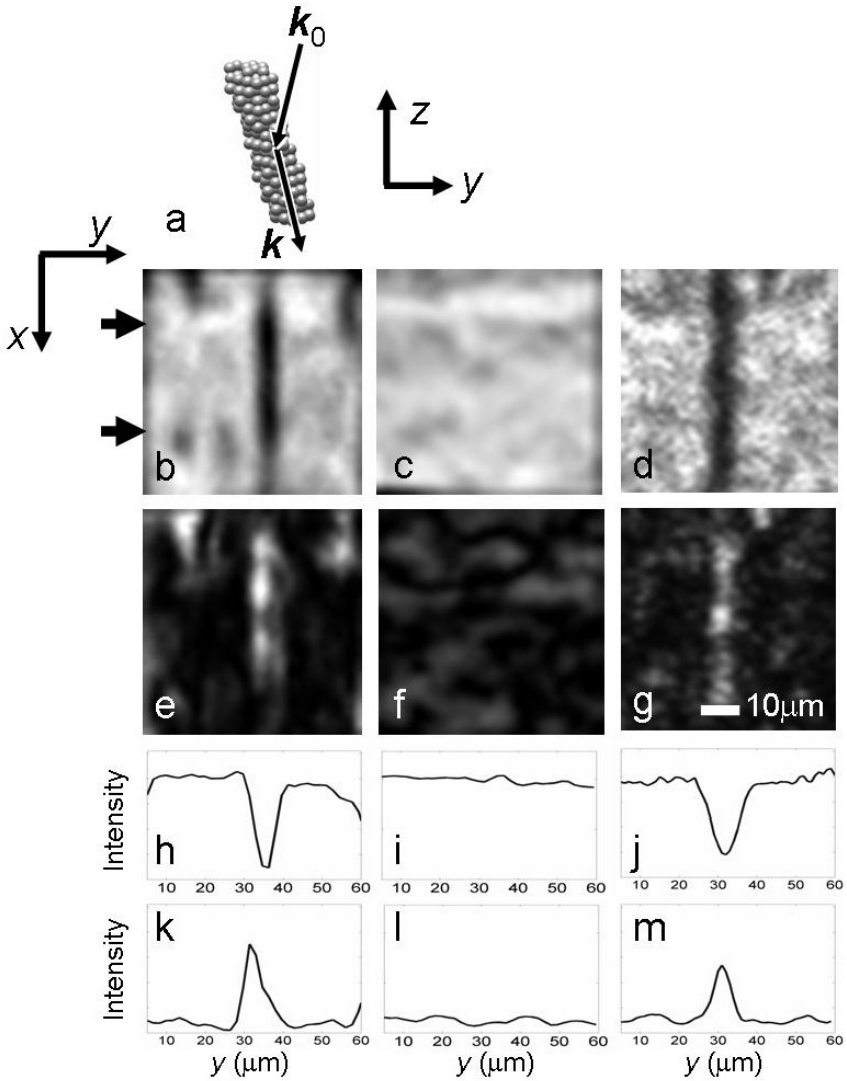

Figure 6.2 Comparison of simulated and experimental laser diffraction image contrast
(a) Schematic showing the directions of the wave vectors $\boldsymbol{k}_0$ and $\boldsymbol{k}$ of the incident and diffracted beams with respect to the crystal column. (b) and (c) Calculated laser diffraction images for s = 0 using the (220) (b) and (2-20) diffraction vectors (c). (d) Experimental laser diffraction image taken at maximum diffracted beam intensity. (e) and (f) Calculated laser diffraction image for s = 0.12 using the (220) (e) and (2-20) diffraction vectors (f). (g) Experimental laser diffraction image taken in a crystal orientation slightly tilted to that used in (d). (h)-(m) Average image intensity as a function of y for all image points within the marked x-interval (arrows) in figure (b).

contrast width is obtained from the average intensity profile as a function of y for all image points within the marked x-interval (arrows in figure 6.2b). The dark line in figure 6.2b corresponds to a drop of the image intensity, whereas the white line in figure 6.2e corresponds to an intensity peak as shown by the intensity curves in figs. 6.2h and k. The width of the defect contrast is determined from the distance Δy between points, at which the intensity has decreased (increased) to half of its minimum (maximum) value. A width of $\Delta y = 6.0$ μm (figs. 6.2 h) is obtained for figure 6.2 b, in good agreement with $\Delta y = 7.0$ μm (figure 6.1 j) obtained from the corresponding experimental image, figure 6.1 d. For the inverted image, a value of 5.1 μm (figure 6.2k) is obtained from figure 6.2e, in reasonable agreement with $\Delta y = 5.6$ μm (figure 6.2 m) measured for the experimental image, figure 6.2g.

Important differences in the imaging of atomic crystals by TEM and colloidal crystals by LDM arise from the different ratio of the wavelength of the imaging radiation to typical

crystal lattice constants: While in TEM, the wavelength of the electron beam is typically 2 orders of magnitude smaller than interatomic distances, the wavelength of the laser beam used for imaging colloidal crystals is only about a factor of two smaller than the distance between particles. As a result, scattering angles are larger, and the resolution limit with respect to the particle size is lower. To estimate the effect of the lower resolution limit on the imaging of dislocations, we compare the size of the first Fresnel zones with the interatomic distances. Since the radius of the first Fresnel zone $r_F \approx \sqrt{\lambda D_F}$, where D_F is the distance between the defect position in the foil and the lower surface of the crystal, the radius of the Fresnel zones at the bottom of the crystal is quite small, but it is large for the upper part of the crystal. For atomic crystals, $r_F \sim 6$Å for layers at the top of a crystal of thickness 1000 Å, while for colloidal crystals, $r_F \sim 5$μm for the top of a 40 μm thick crystal. Since the strain field of the dislocation varies significantly over this distance, the image of dislocations in the upper part of the colloidal crystal is less distinct than of those in the bottom part. The column of radius of 3 μm chosen for the image simulations represents a compromise: columns of this size contain a sufficient number of particles, while still covering a reasonably small distance, on which the dislocation strain field does not vary too much. The resulting images show reasonably smooth contrast, while the defect image is still not smeared out.

7. Conclusions

Visible light offers fascinating possibilities to investigate the structure and dynamics of soft crystals composed of micrometer size constituent particles. This article has focused on optical diffraction contrast imaging and high-resolution optical microscopy to elucidate crystal formation and defect propagation. Optical diffraction techniques give an overview over crystal topologies and defect arrangements on millimeter length scale. Laser diffraction microscopy takes advantage of coherent monochromatic light to analyze defect lattice distortions. In analogy to the transmission electron microscopy technique of conventional crystals this technique provides direct insight into defect mechanisms in soft crystals, thereby contributing to our understanding of this class of materials.

Investigation of defect propagation shows that similar to conventional solids, soft crystals nucleate dislocations at small applied strain to reduce strain energies. The propagation and elastic interactions of these dislocations are well described by continuum models taking into account the ~11 orders of magnitude lower elastic modulus, and the viscous effects due to the suspending solvent. The diffraction contrast of dislocations in soft crystals is described in terms of optical scattering theory and dynamical diffraction theory by applying image simulation techniques developed for transmission electron microscopy. Kinematical theory provides a good approach for optically matched transparent suspensions.

High-resolution imaging with confocal microscopy offers unprecedented detail at the single particle level: Reconstructions of the three-dimensional crystal lattice provide images of defect propagation on the single particle level. Together, laser diffraction and confocal microscopy offer insight into defect dynamics on a range of length scales. This combination of techniques allows us to bridge length scales, thereby offering new opportunities for a multiscale analysis of defect motion in soft materials.

Periodic structures with length scales in the nano- and micrometer range are of increasing importance for applications. Optical diffraction microscopy and its ability to directly visualize defect structures on large length scales can provide important contributions to the characterization of ordered microscale materials, when a high degree of perfection is essential. Furthermore, understanding crystal fomation and defect nucleation in soft systems will drive progress in the development of new soft materials.

The application of confocal microscopy, however, allows us to go much beyond crystalline materials: The ability of three-dimensional reconstruction offers new opportunities

for the investigation of amorphous materials, for which electron microscopy faces fundamental limitations. Particle trajectories determined from three-dimensional reconstructions (Besseling *et al.* 2008) allow insight into the flow of amorphous materials and the glass transition (Schall *et al.* 2007, Weeks *et al.*, 2000). This field is developing at a rapid pace, and new insight and surprises are waiting ahead.

Acknowledgement

I would like to thank Dr. R. Sprik, Prof. A. Howie, Prof. F. Spaepen and Prof. D. Weitz for helpful discussions and feedback on the manuscript. Furthermore, I would like to thank all authors that were willing to allow use of their figures in this review. This work was supported by the Netherlands Organization for Scientific Research (NWO, VIDI award).

References

Aarts D G A L, Schmidt M and Lekkerkerker H N W2004 Direct visual observation of thermal capillary waves *Science* **304** 847–50

Aarts D G A L, Lekkerkerker H N W, Guo H, Wegdam G H and Bonn D 2005 Hydrodynamics of Droplet Coalescence, *Phys. Rev. Lett.* **95** 164503.

Aastuen D J W, Clark N A and Cotter L K 1986 Nucleation and growth of colloidal crystals *Phys. Rev. Lett.* **57**, 1733.

Anderson V J and Lekkerkerker H N W 2002 Insights into phase transition kinetics from colloidal science, *Nature* **416**, 811-5

Auer S and Frenkel D 2001 Prediction of absolute crystal nucleation rate in hard-sphere colloids, *Nature* **409**, 1020-23.

Bawden F C, Pirie N W, Bernal J D and Fankuchen I 1936 Liquid Crystalline Substances from Virus-infected Plants *Nature* **138**, 1051-52.

Bartlett P and Campbell A I 2005 Three-dimensional binary superlattices of oppositely charged colloids *Phys. Rev. Lett.* **95** 128302

Bernal J D and Fankuchen I 1937 Structure Types of protein 'crystals' from virus-infected plants *Nature* **139**, 923-24

Besseling R, Isa L, Weeks E R and Poon W C K Quantitative imaging of colloidal flows *Adv. Coll. Int. Sci.*, in press

Bohren C F and Huffman D R 1998, Absorption and Scattering of Light by Small Particles, John Wiley & Sons, New York, U.S.A.

Bullough R, Maher D M and Perrin R C 1971 Electron Microscope Image Contrast from Dislocation Loops *Phys. Stat. Sol.* B **43**, 689-706.

Campbell A I, Anderson V J, van Duijneveldt J S and Bartlett P 2005 Dynamical arrest in attractive colloids: the effect of long-range repulsion *Phys. Rev. Lett.* **94** 208301

Cheng Z, Russel W B and Chaikin P 1999 Controlled growth of hard-sphere colloidal crystals, *Nature* **401**, 893-95

Cheng Z, Zhu J, Russel W B, and Chaikin P M, 2000 Phonons in an entropic crystal *Phys. Rev. Lett.* **85**, 1460-63.

Clark, N A, Hurd, A J, Ackerson, B J 1979 Single colloidal crystals *Nature* **281**, 57-60.

Cowley J M and Moodie A F 1957 The scattering of electrons by atoms and crystals. I. A new theoretical approach Acta Cryst. 10, 609-19.

Crandall R S and Williams R 1977 *Science* **198**, 293-95

Crocker J C and Grier D G 1996 Methods of Digital Video Microscopy for Colloidal Studies, *J. Coll. Int. Sci.* **179**, 298-310.

Darwin C G 1914 The theory of x-ray reflexion, *Phil. Mag.* **27**, 315 and 675.

de Villeneuve V W A, Miedema P S, Meijer J M and Petukhov A V 2007 Grain size effects on lateral islands in hard-sphere crystals, *Europhys. Lett.* **79**, 56001
Dhont J K G, Smits C, Lekkerkerker H N W 1992 A time resolved static light scattering study on nucleation and crystallization in a colloidal system *J. Colloid Int. Sci.* **152**, 386-401
Dinsmore A D, Weeks E R, Prasad V, Levitt A C and Weitz D A 2001 Three-Dimensional Confocal Microscopy of Colloids, *Applied Optics* **40**, 4152-59
Dinsmore A D, Prasad V, Wong, I Y, Weitz D A 2006 Microscopic Structure and Elasticity of Weakly Aggregated Colloidal Gels *Phys. Rev. Lett.* **96** 185502
Dolbnya, I P, Petukhov A V, Aarts D G A L, Vroege G J and Lekkerkerker H N W 2005 Coexistence of rhcp and fcc phases in hard-sphere colloidal crystals, *Europhys. Lett.* **72**, 962-8
Dubois-Violette E, Pieranski P, Rothen E and Strzelecki L 1980 Shear waves in colloidal crystals: I Determination of the elastic modulus *J. Physique* **41**, 369-76.
Dullens R P A, Aarts D G A L and Kegel W K 2006 Dynamic broadening of the crystal–fluid interface of colloidal hard spheres *Phys. Rev. Lett.* **97** 228301
Edwards O S and Lipson H 1942 Imperfections in the structure of Cobalt I. Experimental work and proposed structure *Proc. Roy. Soc. London* **A180**, 268-77
Elliot M S and Poon W C K 2001 Conventional optical microscopy of colloidal suspensions *Adv. Coll. Int. Sci.* **92**, 133-94.
Eyre B L, Maher D M and Perrin R C 1977 Electron microscope image contrast from small dislocation loops: I. theoretical predictions for edge dislocation loops in a bcc crystal, *J. Phys:*
Flaugh P L, O´Donnell S E, Asher S A 1984 Development of a new optical wavelength rejection filter: demonstration of its utility in Raman spectroscopy *Appl. Spectrosc* **38**, 847-50
Frank F C and van der Merwe J H 1949 One-dimensional dislocations. I Static Theory, *Proc Roy. Soc. (London) A* **198**, 205-25.
Frenkel J, 1926 Zur Theorie der Elastizitaetsgrenze und der Festigkeit kristallinischer Koerper *Z. Phys.* **37**, 572.
Frenkel D and Ladd A J C 1987 Elastic constants of hard-sphere crystals *Phys. Rev. Lett.* **59** 1169.
Gannepalli A and Mallapragada S K 2002 Atomistic studies of defect nucleation during nanoindentation of Au(001) *Phys. Rev. B* **66**, 104103
Gans R 1925 Strahlungsdiagramme ultramikroskopischer Teilchen *Ann. Physik*, **381**, 29-38.
Gasser U, Weeks E R, Schofield A, Pusey P N and Weitz D A 2001 Real-space imaging of nucleation and growth in colloidal crystallization *Science* **292** 258–62
Gast, A P and Monovoukas, Y 1991 A new growth instability in colloidal crystallization, *Nature* **351**, 553-5.
Gouldstone A, Koh H J, Zeng, K Y, Giannakopoulos, A E and Suresh S 2000 Discrete and continuous deformation during nanoindentation of thin films, *Acta Mater.* **48**, 2277-95.
Gu M 1996 *Principles of three-dimensional imaging in confocal microscopes*, World Scientific, Singapore.
Haasen P 1978 *Physical Metallurgy*, Cambridge University Press, Cambridge, U.K.
Harland J L, Henderson S I, Underwood S M and van Megen W 1995 Observation of Accelerated Nucleation in Dense Colloidal Fluids of Hard Sphere Particles, *Phys. Rev. Lett.* **75**, 3572-75.
Haw M D, Poon W C K and Pusy P N 1998 Direct observation of shear-induced order in colloidal suspensions *Phys. Rev. E* **57** 6859-64.
He Y, Olivier B and Ackerson B J 1997 Morphology of crystals made of hard spheres *Langmuir* **13**, 1408-12.
Heidenreich R D 1949 Electron Microscope and diffraction study of metal crystal textures by means of thin sections *J. Appl. Phys.* **20**, 993-1010.

Hertz H J 1881 Über die Berührung fester elastischer Körper *J. reine angew. Math.* **92**, 156. Reprinted in an English translation in Hertz's ´Miscellaneous Papers´. London: Macmillan.
Hiltner, A and Krieger, I M 1969 Diffraction of light by ordered suspensions, *J. Phys. Chem.* **73**, 2386-89.
Hirsch P B, Howie A and Whelan M J 1960 A kinematical theory of diffraction contrast of electron transmission microscope images of dislocations and other defects, *Phil. Trans. A*, **252**, 499-529.
Hirsch P B Howie A Nicholson R B Pashley D W and Whelan M J 1965 *Electron microscopy of thin crystals*, Butterworth, London.
Hirth J P 1963 The influence of surface structure on dislocation nucleation, in: *The Relation between the structure and the mechanical properties of metals*, Proceedings of the conference at the National Physical Laboratory, Teddington, Middlesex, Her Majesty's Stationary Office, London, 217-28.
Hirth J P and Lothe J 1982 *Theory of dislocations* Wiley, New York.
Hoover W G, Ree, F M, 1968, Melting Transition and Communal Entropy for Hard Spheres, *J. Chem. Phys.* **49**, 3609.
Hoogenboom J P, Derks D, Vergeer P, van Blaaderen A 2002 Stacking faults in colloidal crystals grown by sedimentation, *J. Chem. Phys.* **117**, 11320-28
Hoogenboom J P, van Langen-Suurling A K, Romijn J and van Blaaderen A 2004 Epitaxial growth of a colloidal hard-sphere hcp crystal and the effect of epitaxial mismatch on crystal structure *Phys. Rev.* E **69** 051602
Howie A and Whelan M J 1961 Diffraction Contrast of Electron Microscope Images of Crystal Lattice Defects. II. The Development of a Dynamical Theory, *Proc. Roy. Soc. A*, **263**, 217-37.
Howie A and Whelan M J 1962 Diffraction contrast of electron microscope images of crystal lattice defects. III. Results and experimental confirmation of the dynamical theory of dislocation image contrast *Proc. Roy. Soc. A*, **267**, 206-230.
Hull D and Bacon D J 2001 *Introduction to dislocations*, 4th edition, Butterworth-Heinemann, Oxford, U.K.
Hull R and Bean J C 1992 Misfit dislocations in lattice-mismatched epitaxial films, *Critical Reviews in Solid State and Materials Science* **17**, 507-46.
Hunt N, Jardine R and Bartlett P 2000 Superlattice formation in mixtures of hard-sphere colloids, *Phys. Rev. E* **62** 900-913.
Hurd A J, Clark N A, Mockler R C and O´Sullivan W 1982 Lattice dynamics of collidal crystals *Phys. Rev. A* **26** 2869-81.
Iler R K 1965 Formation of precious opal *Nature* **207**, 472-73.
Jackson J D 1999 *Classical Electrodynamics*, John Wiley and Sons, Inc., Hoboken, U.S.A.
Joannopoulos J D, Johnson S G, Winn J N and Meade R 2008 *Photonic Crystals: Molding the flow of light*, 2nd edition, Princeton University Press, Princeton, New Jersey.
Johnston W G and Gilman J J 1959 Dislocation velocities, dislocation densities and plastic flow in lithium fluoride crystals *J. Appl. Phys.* **30**, 129.
Jorand M, Rothen F Pieranski P 1985 Dislocation motion in colloidal crystals *J. Physique* **C3**, 245-55.
Krauz A S and Krauz K 1996. *Unified Constitutive Laws of Plastic Deformation*, Academic Press, New York.
Kegel W K and van Blaaderen A 2000 Direct observation of dynamical heterogeneities in colloidal hard-sphere suspensions *Science* **287** 290–3
Keim P, Maret G, Herz U and von Grünberg H H 2004 Harmonic Lattice Behavior of Two-Dimensional Colloidal Crystals, *Phys. Rev. Lett.* **92**, 215504.
Kelchner C L, Plimpton S J, Hamilton J C 1998a Dislocation nucleation and defect structure during surface indentation *Phys. Rev. B* **58** 11085-8

Kelchner C L, Plimpton S J, Hamilton J C 1998b Dislocation nucleation and defect structure during surface indentation *Phys. Rev. B* **58** 11085-8
Kikuchi S 1928 Diffraction of cathode rays by mica *Jap. J. Phys.* **5**, 83.
Kiritani M 1997 Story of stacking fault tetrahedra *Materials Chemistry and Physics* **50**, 133-8
Knap J and Ortiz M 2003 Effect of Indenter-Radius Size on Au(001) Nanoindentation *Phys. Rev. Lett.* **90** 226102.
Kose A, Ozaki M, Takano K, Kobayashi Y and Hachisu S 1973 Direct observation of ordered latex suspension by metallurgical microscope *J. Coll. Int. Sci.* **44**, 330-38.
Leunissen M E, Christova C G, Hynninen A P, Royall C P, Campbell A I, Imhof A, Dijkstra M, van Roij R and van Blaaderen A 2005 Ionic colloidal crystals of oppositely charged particles *Nature* **437** 235–40
Li J, Van Vliet, K J, Zhu T, Yip S and Suresh S, 2002 Atomistic mechanisms governing elastic limit and incipient plasticity in crystals *Nature* **418**, 307-10.
Lilleodden E T, Zimmerman, J A, Foiles, S M and Nix W D 2003 Atomistic simulations of elastic deformation and dislocation nucleation during nanoindentation, *J. Mech. Phys. Solids* **51** 901-920.
Lindsay H M and Chaikin P M 1982 Elastic properties of colloidal crystals and glasses *J. Chem. Phys.* **76**, 3774-81.
Lord Rayleigh, 1871a On the light from the sky, its polarization and color *Phil. Mag.* **41**, 107.
Lord Rayleigh, 1871b On the scattering of light by small particles *Phil. Mag.* **41**, 447.
Lord Rayleigh 1881 *Phil. Mag.* **12**, 81
Lu P J 2005 Confocal Scanning Optical Microscopy and Nanotechnology in *Handbook of Microscopy for Nanotechnology*, N. Yao, and Z. L.Wang, eds. Kluwer, 3-24.
Lu P J, Conrad J C,Wyss H M, Schofield A B andWeitz D A 2006 Fluids of clusters in attractive colloids *Phys. Rev. Lett.* **96** 028306
Luck, W. Klier, M., and Wesslau, H. 1963a *Ber. Bunsenges. Phys. Chem.* 67, 75, 84.
Luck, W. Klier, M., and Wesslau, H. 1963b *Naturwissenschaften* 50, 485.
Maher D M, Perrin R C and Bullough R, 1971, Computer Simulation of Electron Microscope Images, *Phys. Stat. Sol.* B **43**, 707-15.
Marcinkowski M J and Sree Harsha K S 1968 Properties of finite circular dislocation glide loops *J. Appl. Phys.* **39**, 1775-83.
Markos P and Soukoulis C M 2008 *Wave Propagation: From Electrons to Photonic Crystals and Left-Handed Materials*, Princeton University Press, Princeton, New Jersey.
Matthews J W, Mader S and Light T B 1970 Accommodation of Misfit Across the Interface Between Crystals of Semiconducting Elements or Compounds *J. Appl. Phys.* **41**, 3800.
Matthews J W and Blakeslee A E 1974 Defects in epitaxial multilayers. I Misfit dislocations *J. Cryst Growth* **27**, 118-125.
Meijer J-M, de Villeneuve V W A and Petukhov, A V 2007 In-plane stacking disorder in polydisperse hard sphere crystals, *Langmuir* **23**, 3554-60
Mie G 1908 Contribution to the Optical Properties of Turbid Media, Especially of Colloidal Solutions of Metals *Ann. Physik*, **25**, 377-91.
Mills M J, Daw M S and Foiles S M 1994 High-resolution transmission electron microscopy studies of dislocation cores in metals and intermetallic compounds *Ultramicroscopy* **56**, 79-93
Minor A M, Lilleodden E T, Stach E A and Morris J W 2002 In-Situ Transmission electron microscopy study of the nanoindentation behavior of Al, J Electronic Materials 31, 958-64.
Minor A M, Asif, S A S, Shan Z, Stach E A, Cyrankowski E, Wyrobek T and Warren O L 2006 A new view of the onset of plasticity during the nanoindentation of aluminum, Nature Materials 5, 697-702.
Minsky M 1988 Memoir on inventing the confocal scanning microscope *Scanning* **10**, 128-38.

Mitaku S, Ohtsuki T, Enari K, Kishimoto A and Okano K 1978 *Japan. J. Applied Physics* **17**, 305.
Monovoukas Y, Gast A P 1989 The experimental phase diagram of charged colloidal suspensions *J. Colloid Int. Sci.* **128**, 533-48.
Monovoukas, Y and Gast A P 1990a Microstructure identification during crystallization of charged colloidal suspensions *Phase transitions* **21**, 183-95.
Monovoukas Y, Fuller G G and Gast A P 1990b Optical anisotropy in colloidal crystals *J. Chem. Phys.* **93**, 8294-99.
Monovoukas, Y and Gast A P, 1991, A study of colloidal crystal morphology and orientation via polarizing microscopy, *Langmuir* **7**, 460-68.
Nabarro F R N 1947 Dislocations in a simple cubic lattice *Proc. Phys. Soc.* **59**, 256-72.
Murray C A and Grier D G 1996 Video microscopy of monodisperse colloidal systems *Ann. Rev. Phys. Chem.* **47**, 421-62.
Okuba T 1994 Macro-ion Characterization: from dilute solution to complex fluids (ACS symposium series 548) ed K S schmitz, p 364
Palberg, T. 1999 Crystallization kinetics of repulsive colloidal spheres *J. Phys.: Condens. Matter* **11**, R323-R360.
Pawley J B 1995 *Handbook of Biological Confocal Microscopy* (New York: Plenum)
Pham K N, Puertas A M, Bergenholtz J, Egelhaaf S U, Moussaid A, Pusey P N, Schofield A B, Cates M E, Fuchs M and Poon W C K 2002 Multiple glassy states in a simple model system *Science* **296** 104–6
Peach M and Koehler J S 1950 The Forces exerted on dislocations and the stress field produced by them Phys. Rev. 80, 436-39.
Peierls R E 1940 The size of a dislocation *Proc. Phys. Soc.* **52**, 34-37.
Pertsinidis A and Ling X S 2001a Diffusion of point defects in two-dimensional colloidal crystals *Nature* **413**, 147-50.
Pertsinidis A and Ling X S 2001b Equilibrium Configurations and Energetics of Point Defects in Two-Dimensional Colloidal Crystals *Phys. Rev. Lett.* **87**, 098303
Pertsinidis A and Ling X S 2005 Video microscopy and micromechanics studies of one- and two-dimensional colloidal crystals *New J. Phys.* **7,** 33
Pieranski P, Strzelecki L and Friedel J 1979 Observation of edge dislocations in ordered polystyrene latexes *J. Physique* **40**, 853-59.
Pieranski P 1980 Two-dimensional interfacial colloidal crystals *Phys. Rev. Lett.* **45**, 569-72.
Pieranski P, 1981, Defects in three-and two-dimensional colloidal crystals Les Houches, Session XXXV, 1980 – Physics of defects, R. Balian et al. eds., North Holland Publishing Company, 183-200.
Pieranski P, Dubois-Violette E, Rothen F, and Strzelecki L 1981 Geometry of Kossel lines in colloidal crystals *J. Physique* **42**, 53-60.
Pieranski P 1983 Colloidal Crystals *Contemp. Phys.* **24**, 25-72.
Pinsker Z G, *Dynamical Scattering of X-Rays in Crystals* (Springer Ser. Solid State Sci. Vol. 3 (Springer, Berlin, Heidelberg 1978)
Prasad V, Semwogerere D, Weeks E R 2007 Confocal microscopy of colloids *J. Phys.: Condens. Matter* **19**, 113102.
Pronk S and Frenkel D 1999 Can stacking faults in hard-sphere crystals anneal out spontaneously? *J. Chem. Phys.* **110** 4589-92
Pusey P N and van Megen, W 1986 Phase behavior of concentrated suspensions of nearly hard colloidal spheres *Nature* **320**, 340-42.
Pusey P N, van Megen W, Bartlett P, Ackerson B J, Rarity J G, Underwood S M 1989 Structure of crystals of hard colloidal spheres *Phys. Rev. Lett.* **63**, 2753-56
Reimer L 1993 *Transmission electron microscopy, Physics of image formation and microanalysis*, Springer series in optical sciences volume 36, Springer, Berlin.

Reinke D, Stark H, von Grünberg H-H, Schofield A B, Maret G and Gasser U 2007 Noncentral forces in crystals of charged colloids, *Phys. Rev. Lett.* **98**, 038301.
Rogers B R and Lagerlöf K P D 2008a Crysllography of ordered colloids using optical microscopy. 1. Parallel-beam technique Applied Optics 47, 284-95.
Rogers B R and Lagerlöf K P D 2008b Crysllography of ordered colloids using optical microscopy. 2. Divergent-beam technique, Applied Optics 47, 1867-79.
Rundquist, P.A., Photinos, P., Jagannathan, S., and Asher, S.A. 1989 Dynamical Bragg diffraction from crystalline colloidal arrays *J. Chem. Phys.* **91** (8), 4932-41.
Rundquist P A, Kesavamoorthy R, Jagannathan S and Asher S A 1991 Thermal diffuse scattering from colloidal crystals, *J. Chem. Phys.* **95**, 1249-57.
Russel, W B, Chaikin P M, Zhu J, Meyer, W V and Rogers, R 1997 Dendritic growth of hard sphere crystals *Langmuir* **13**, 3871-3881.
Saldin D K and Whelan M J 1979a The construction of displacement fields of dislocation loops and stacking-fault tetrahedra from angular dislocation segments, *Phil. Trans. A*, **292**, 513-21.
Saldin D K, Stathopoulos A Y and Whelan M J, 1979b Electron microscope image contrast of small dislocation loops and stacking-fault tetrahedra, *Phil. Trans. A*, **292**, 523-37.
Sanders J V 1964 Colour of precious opal, *Nature* **204**, 1151-53.
Schall P, Cohen I, Weitz D A and Spaepen F 2004 Visualization of dislocation dynamics in colloidal crystals *Science* **305** 1944–8
Schall P, Cohen I, Weitz D A and Spaepen F 2006 Visualizing dislocation nucleation by indenting colloidal crystals *Nature* **440** 319–23
Schall P, Weitz D A and Spaepen F 2007 Structural rearrangements that govern flow in colloidal glasses, *Science* **318**, 1895-9.
Schäublin R, Almazouzi A, Dai Y, Osetsky Yu N and Victoria M 2000 Quantitative analysis of CTEM images of small dislocation loops in Al and stacking fault tetrahedra in Cu generated by molecular dynamics simulation, *J Nucl. Mater.* **276**, 251-57.
Schofield A B, Pusey P N and Radcliff P 2005 Stability of the binary colloidal crystals AB_2 and AB_{13} *Phys. Rev. E* **72** 031407.
Schuh C A 2006 Nanoindentation studies of materials, *Materials Today* **9**, 32-39
Sheppard C J R and Shotton D M 1997 *Confocal Laser Scanning Microscopy*, Springer, New York
Simeonova, N B, Dullens, R P A, Aarts D G A L, de Villeneuve, V W A, Lekkerkerker H N W, Kegel, W K, 2006 Devitrification of colloidal glasses in real space *Phys. Rev. E* **73**, 041401
Sirota E B, Ou-Yang H D, Sinha, S K and Chaikin P M 1989 Complete phase diagram of a charged colloidal system: a synchrotron x-ray scattering study, *Phys. Rev. Lett.* **62**, 1524-27.
Solomon T and Solomon M J 2006 Stacking fault structure in shear-induced colloidal crystallization, *J. Chem. Phys.* **124**, 134905
Spry, R.J., and Kosan, D.J. 1986 Theoretical Analysis of the crystalline colloidal array filter *Appl. Spectrosc.* **40**, 782-84.
Suresh S, Nieh, T G, Choi, B W 1999 Nano-indentation of copper thin films on silicon substrates *Scripta Mater.* **41**, 951-57.
Taylor G I 1934 Mechanism of plastic deformation in crystals *Proc. Roy. Soc.* A **145**, 362.
Trappe V, Prasad V, Cipelletti L, Segre P N andWeitz D A 2001 Jamming phase diagram for attractive particles *Nature* **411** 772–5
van Blaaderen A, Imhof A, Hage W and Vrij A 1992 Three-Dimensional Imaging of Submicrometer Colloidal Particles in Concentrated Suspensions Using Confocal Scanning Laser Microscopy, *Langmuir* **8**, 1514-7
van Blaaderen A and Wiltzius P 1995 Real-space structure of colloidal hard-sphere glasses *Science* **270** 1177–79

van Blaaderen A, Ruel R and Wiltzius P 1997 Template-directed colloidal crystallization *Nature* **385**, 321-24
Van de Hulst H C 1981 *Light Scattering by small particles* Dover publications, Mineola, U.S.A.
Verhaegh N A M, van Duijneveld J S, van Blaaderen A and Lekkerkerker H N W 1995 Direct observation of stacking disorder in a colloidal crystal, *J Chem. Phys.* **102**, 1416-1421.
Weeks E R, Crocker J C, Levitt A C, Schofield A and Weitz D A 2000 Three-dimensional direct imaging of structural relaxation near the colloidal glass transition *Science* **287** 627–31
Wette P, Schöpe H-J, Liu J and Palberg T 2003 Solidification in model systems of spherical particles with density-dependent interactions, *Europhys. Lett.* **64**, 124-30
Whelan M J and Hirsch P B 1957a Electron diffraction from crystals containing stacking faults: I *Phil. Mag.* **2**, 1121-42
Whelan M J and Hirsch P B 1957b Electron diffraction from crystals containing stacking faults: II *Phil. Mag.* **2**, 1303-24
Williams D B and Carter C B 1996 Transmission electron microscopy: a textbook for materials science, Vol. 1-4, Plenum Press, New York, U.S.A.
Williams R and Crandal R S 1974 The structure of crystallized suspensions of polystyrene spheres *Physics Letters* **48A**, 225-26
Williams R, Crandall R S and Wojtowicz P J 1976 Melting of crystalline suspensions of polystyrene spheres *Phys. Rev. Lett.* **37**, 348-51
Wilson A J C 1942 Imperfections in the structure of Cobalt II. Mathematical treatment of the proposed structure *Proc. Roy. Soc. London* **A180**, 277-85
Würth M, Schwarz J, Culis F, Leiderer P and Palberg T 1995 Growth kinetics of body centered cubic colloidal crystals *Phys. Rev. E* **52**, 6415-23
Yoshida H, Ito K and Ise N 1991 Localized ordered structure in polymer latex suspensions as studied by a confocal laser scanning microscope *Phys. Rev.* B **44** 435–8
Zachariasen, W H 1945 *Theory of X-Ray Diffraction in Crystals*, Wiley, New York
Zahn K and Maret G 2000 Dynamic Criteria for Melting in Two Dimensions, *Phys. Rev. Lett.* **85**, 3656-59.
Zahn K, Wille A, Maret G, Sengupta S and Nielaba, 2003 Elastic Properties of 2D Colloidal Crystals from Video Microscopy, *Phys. Rev. Lett.* **90**, 155506.
Zhu J, Rogers R, Meyer W, Ottewill R H, STS-73 Space Shuttle Crew, Russel W B and Chaikin P M 1997 Crystallization of hard-sphere colloids in microgravity *Nature* **387**, 883-5.